A phase-field approach to model fracture of arterial walls: Theory and finite element analysis

Osman Gültekin[a], Hüsnü Dal[b], Gerhard A. Holzapfel[a,*]

[a] *Institute of Biomechanics, Graz University of Technology, Stremayrgasse 16/II, 8010, Graz, Austria*
[b] *Department of Mechanical Engineering, Middle East Technical University, Dumlupınar Bulvarı No. 1, Çankaya, 06800, Ankara, Turkey*

Abstract

This study uses a recently developed phase-field approach to model fracture of arterial walls with an emphasis on aortic tissues. We start by deriving the regularized crack surface to overcome complexities inherent in sharp crack discontinuities, thereby relaxing the acute crack surface topology into a diffusive one. In fact, the regularized crack surface possesses the property of Gamma-Convergence, i.e. the sharp crack topology is restored with a vanishing length-scale parameter. Next, we deal with the continuous formulation of the variational principle for the multi-field problem manifested through the deformation map and the crack phase-field at finite strains which leads to the Euler–Lagrange equations of the coupled problem. In particular, the coupled balance equations derived render the evolution of the crack phase-field and the balance of linear momentum. As an important aspect of the continuum formulation we consider an invariant-based anisotropic constitutive model which is additively decomposed into an isotropic part for the ground matrix and an exponential anisotropic part for the two families of collagen fibers embedded in the ground matrix. In addition we propose a novel energy-based anisotropic failure criterion which regulates the evolution of the crack phase-field. The coupled problem is solved using a one-pass operator-splitting algorithm composed of a mechanical predictor step (solved for the frozen crack phase-field parameter) and a crack evolution step (solved for the frozen deformation map); a history field governed by the failure criterion is successively updated. Subsequently, a conventional Galerkin procedure leads to the weak forms of the governing differential equations for the physical problem. Accordingly, we provide the discrete residual vectors and a corresponding linearization yields the element matrices for the two sub-problems. Finally, we demonstrate the numerical performance of the crack phase-field model by simulating uniaxial extension and simple shear fracture tests performed on specimens obtained from a human aneurysmatic thoracic aorta. Model parameters are obtained by fitting the set of novel experimental data to the predicted model response; the finite element results agree favorably with the experimental findings.

© 2016 Elsevier B.V. All rights reserved.

* Corresponding author.
E-mail address: holzapfel@tugraz.at (G.A. Holzapfel).

1. Introduction

Over the last decades the physiological and pathological aspects of arterial tissues have become a prominent research topic in continuum and computational mechanics in regard to constitutive modeling, damage and fracture mechanics since there exists a salient relation between the histological architecture and the mechanical behavior of arteries in response to loading. As such, ever increasing number of studies have been a fashion to allow the latest advances in the complex structural composition of the arterial wall to be embodied into models which can mimic the mechanical behavior of the tissue in a computer environment.

1.1. Histology and mechanical behavior of arterial walls, related diseases

The arterial wall consists of three distinct layers: the intima (tunica intima), the media (tunica media) and the adventitia (tunica externa). In healthy young individuals the innermost layer, the intima, is composed of a single layer of endothelial cells, and hence has a negligible contribution to the mechanical behavior of the arterial wall. However, due to the development of the sub-endothelial layer with age it thickens and stiffens (arteriosclerosis) so that the mechanical contribution may become significant. The middle layer, the media, involves smooth muscle cells, elastin and collagen fibers arranged in several sub-laminae operating as the main load bearing layer under physiological conditions. The outermost layer, the adventitia, comprises fibroblasts, fibrocytes, and bundles of collagen fibers. Fibroblasts are the cells responsible for secreting elastin and collagen. The adventitia is the main functioning layer under supra-physiological loading conditions to prevent the artery from rupture [1].

Subsequently, we cast a closer look into the structural, mechanical and functional characteristics of the constituents that emanate from their composition and orientation in the arterial wall. The endothelial cells, e.g., assume a spindle shape when subjected to shear stress as a result of blood flow and convey this mechanical stimuli to smooth muscle cells which regulate the diameter of the artery [2]. The long molecules of elastin compose a rubber-like network having cross-links with each other. They can be stretched about 2.5 times their initial length and keep the original size of the artery upon a stretch or contraction [3]. The structural protein collagen, however, emerges as the main load carrying constituent among all. Collagen molecules, called tropocollagens, organize themselves into collagen fibrils through intermolecular cross-links. These fibrils assemble into collagen fibers by proteoglycans (PGs). The orientation of the collagen fibers in both the media and the adventitia renders a helical structure [1]. To give an overall idea in regard to the mechanical contribution of cross-links to the tissue, it is observed that the fibrillar stretch is about one order of magnitude smaller than the macroscopic stretch [4]. Type I and III are the most common types of collagen in arterial walls [5]. In the absence of load, collagen fibers appear wavy and in a crimped form. When the load is present they gradually straighten and further elongate as the load increases. In fact, they exhibit a J-like stress–strain behavior [6]. Furthermore, similar to ropes, they cannot withstand compressive forces.

With regard to constitutive models to characterize the mechanical behavior of the arterial wall, the model considerations have followed a propensity from being isotropic thin-walled to anisotropic thick-walled at finite deformation, as can be found in, e.g., [7–9] among others. Their applicability is limited due to the lack of either convexity or anisotropy. Besides, [9] can only recover special types of deformation as being two-dimensional. All of those aforecited models with their variants are essentially purely phenomenological. Another constitutive approach, blended with anisotropy and polyconvexity, was suggested in [1]. It was developed on the basis of a thick-walled tube which assumes an incompressible solid. The micro-structural information was partly imparted by this model. It was later modified to take account of an axisymmetric model of collagen fiber dispersion [5] and a non-symmetric collagen fiber dispersion [10]. Aside from the aforementioned set of models, it is noteworthy to refer to a different (debatable) model approach namely to use worm-like chains to capture the mechanical response of biological tissues, i.e. [11,12]; for a review concerned with the mathematical modeling of the mechanical properties of soft biological tissues that constitute arterial walls, see [13].

Considering diseases that trigger a cascade of mechanically degenerative processes we hereby address some general aspects of aneurysm, atherosclerosis and aortic dissection which eventually may result in the fracture of the wall. Aneurysms can be viewed as a local dilation of the aorta forming a balloon-like bulge on the localized part of the wall upon the onset of aneurysm. The stress acting on this localized part increases while the wall strength experiences degradation. The fracture happens if the dilated aortic wall cannot carry the wall tension due to hemodynamic loads which may bring fatal consequences. The primary factors causing aneurysms are known to be aging, smoking,

hypertension, atherosclerosis and genetic disorders [14,15]. The fact that atherosclerosis have turned out to be a prevailing cause of casualties draws the attention of modern medical science. The formation of atherosclerotic plaques is attributed to the low wall (laminar) shear stress associated with the disrupted laminar blood flow which forms a breeding ground for the fibroinflammatory lipid plaque. This plaque gradually grows and narrows the lumen of the artery; causes also adverse changes in the mechanical properties i.e. fibrotic media loses its elasticity considerably and rupture can be induced by the increase of blood pressure in case of an excessive atherosclerotic plaque [16–18]. Aortic dissections commence with an initial tear in the intima which advances further in the radial direction towards the media. The dissection propagates later in the axial direction owing to blood flow while it retains to be located on the sub-adventitial plane (between the sub-layers of media or media and adventitia) which creates a false lumen that can entirely close off the lumen of the aorta [19].

1.2. Damage and fracture models in arterial walls

To the best of our knowledge, there are only a few endeavors to model failure of arterial walls. The study [20] implemented the XFEM (Extended Finite Element Method), a technique to model crack growth without re-meshing, on the basis of PUFEM (Partition of Unity Finite Element Method) which allows the local enrichment functions, i.e. Heaviside functions, associated with additional degrees of freedom to be integrated into a finite element approximation [21–23]. In [20] the authors showed a numerical analysis of a peeling experiment (mode-I) on a dissected aortic medial strip in the form of delamination. Later on, the study [24] documented the simulation of the fracture of an atherosclerotic arterial wall in three-dimension by using an anisotropic extension of the irreversible isotropic cohesive element model, as proposed in [25]. The surface-like cohesive elements are inserted between two solid elements where the crack is expected to grow and the opening displacements are resisted by cohesive tractions. Next, the study [26] performed the identical numerical test as in [20] and compared the results with various mesh sizes. A recently developed phase-field model for fracture, on which we will give a detailed background information in the forthcoming section, applied to the arterial wall, is documented in [27]. However, the compressive stiffness attributed to collagen fibers in the free-energy function utilized in [27] was not physically justified, inasmuch as it is a well accepted practice within the biomechanics community that collagen fibers are not regarded as compression-resistant elements. Subsequently, they employed this model on two-dimensional numerical examples. A visual comparison of the overall crack growth between the simulation results (Fig. 12(a)) and the typical experimental test results (Figure 5 in [18]) suggests a conspicuous discrepancy. In addition to the abovementioned continuum models there are some multi-scale approaches available, [28,29], to model the failure of biological tissues by connecting the micro-scale failure of individual collagen fibers with the macro-scale material response.

Apart from the fracture phenomenon, [30] modeled stress-softening behavior evident in cyclic tension tests of arterial walls by applying continuum damage mechanics (CDM), see [31], with $(1-d)$ inserted only in the anisotropic part of the hyperelastic function i.e. damage solely occurs in fibers. [32] extended the approach by postulating a stochastic method to account for the sliding of the PG bridges that connect collagen fibrils, and speculated that they are responsible for the damage evolution in arterial walls. A recent study by [33] introduced a three-dimensional relaxed incremental variational damage model, thereby convexifying the energy in case of a loss of convexity with a convex hull due to [34].

1.3. Crack phase-field approach to fracture

Fracture, in general, is accompanied by a series of irreversible inhomogeneous micro-mechanisms where a number of imperfections initiated at micro level, i.e. voids and cracks, grow in a particular way in the course of time to form macro-voids and macro-cracks which gives rise to the accumulation of damage in advance of the fracture. This can be realized as a material deterioration by means of stress softening [35].

The authors of [36,37] laid the foundations of the classical theory of brittle fracture with well-known shortcomings to determine curvilinear crack paths, crack kinking and branching angles. These problems regarding the Griffith theory can be eliminated through variational principles due to an energy minimization, as introduced in a phase-field model for a quasi-static brittle fracture in [38], and with the numerical implementation in [39] that approximates the Mumford–Shah functional [40] with a framework rendered by the Γ-convergence theory. This theory tracks the behavior of the global minimum of problems (minimum values and minimizers) by 'integrating out' the local
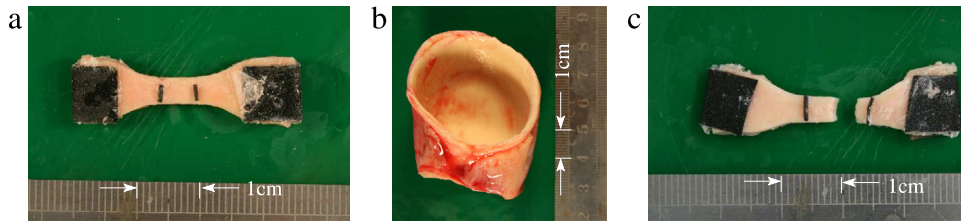
Fig. 1. (a) Intact strip of the media prepared for a uniaxial extension test; (b) segment of a human aneurysmatic thoracic aorta from which the strip was cut out; (c) ruptured strip after the test.

minimizers in the limit [41]. For a comprehensive overview we refer to [42]. The hallmark of all the aforementioned considerations is to provide a diffusive crack topology, healing the sharp crack surface, which approximates between intact and cracked states of the material by means of a scalar assisting variable. Aside from that, the study documented in [43] independently applied a phase-field approach to the brittle fracture based on the Ginzburg–Landau type of evolution equation.

All the above stated approaches suffer from being either unrealistic in the sense that a crack is driven both in tension and compression or they are thermodynamically inconsistent. An alternative quasi-static small strain phase-field model (second-order phase-field theory) of fracture has been presented in [44] with the property of being thermodynamically consistent and allowing crack growth only in tension. Accordingly, this proposed approach handles an incremental variational setup for a two-field problem of gradient-type dissipative solids with a characteristic length scale. From the modeling point of view, this model is conceptually in accordance with CDM. A finite strain extension of this model, as discussed in Section 1.2, can be found in [45,27]. There are also studies dealing with higher order phase-field models (fourth-order phase-field theory) of the strongly anisotropic fracture which resorts to the extended Cahn–Hilliard framework [46].

If we reveal a noticeable advantage of the crack phase-field approach to those approaches outlined in Section 1.2, we can state that crack phase-field models avoid the modeling of discontinuities, whereas the models listed in Section 1.2 try to model discontinuities by means of nodal enrichment techniques using PUFEM or re-meshing strategies which make them a costly task to handle, especially, three-dimensional domains.

In our present contribution, we basically follow the quasi-static brittle fracture model documented in [44,47] where a robust operator-splitting algorithm is implemented. Nevertheless, instead of an incremental formulation we present a continuous formulation of the variational principle for the multi-field problem manifested through the deformation map and the crack phase-field at finite deformations. Besides, we consider the crack growth being driven by a novel energy-based anisotropic failure criterion in accordance with the mechanics of arterial tissues. Furthermore, unlike [27], the represented numerical simulations are carried out in the three-dimensional domain. As a matter of fact, we simulate the fracture of an aortic aneurysmatic tissue specimen undergoing both uniaxial extension and simple shear loads and compare the results with a novel experimental study recently conducted in [48].

To provide a motivation of the present study in a nutshell, Fig. 1(a) displays a medial strip of a human aneurysmatic thoracic aorta sample prepared for a uniaxial extension test, while Fig. 1(b) shows the segment of the thoracic aorta from which the strip was cut out. Fig. 1(c) displays the ruptured strip after the extension test whereby the constitutive and computational modeling of tissue failure is requested.

1.4. Organization of the work

The article is organized as follows. In Section 2 we introduce the field variables governing the coupled problem with corresponding finite strain kinematics. Additionally, the Ginzburg–Landau type phase-field model is motivated both in one and three dimensions. In Section 3 we outline the continuous formulation of the variational framework for the coupled two-field problem by obtaining the strong form of balance equations, also called Euler–Lagrange equations, based on power balance. Section 4 is concerned with the incorporation of an anisotropic hyperelastic constitutive model to delineate the mechanical behavior of the wall in the Eulerian framework. In the sequel, we propose an energy-based anisotropic failure criterion where a critical fracture energy scaled by the length-scale parameter, i.e. the width required to have a smooth approximation of the crack, controls the evolution of the crack phase-field with respect to the isotropic and the anisotropic part of the effective free-energy function. With this setup at hand in
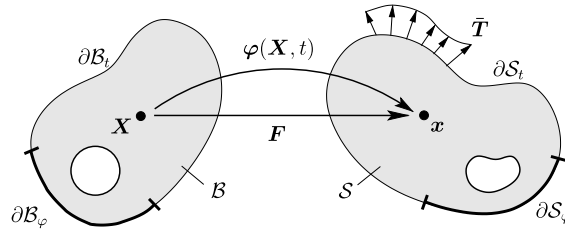
Fig. 2. Nonlinear deformation of a solid. The reference configuration $\mathcal{B} \in \mathbb{R}^3$ and the spatial configuration $\mathcal{S} \in \mathbb{R}^3$. $\boldsymbol{\varphi} : \mathcal{B} \times \mathbb{R} \mapsto \mathbb{R}^3$ is the nonlinear deformation map which maps at time $t \in \mathbb{R}_t$ material point position $\boldsymbol{X} \in \mathcal{B}$ onto spatial position $\boldsymbol{x} = \boldsymbol{\varphi}(\boldsymbol{X}, t) \in \mathcal{S}$. The deformation gradient $\boldsymbol{F}$ maps a Lagrangian line element $\mathrm{d}\boldsymbol{X}$ onto its Eulerian counterpart $\mathrm{d}\boldsymbol{x} = \boldsymbol{F}\mathrm{d}\boldsymbol{X}$.

Section 5 we perform a staggered solution update that partitions the monolithic solution scheme into two sub-problems which contain minimizers for each partial problem. Subsequently, we obtain the weak form of the balance equations by means of a standard Galerkin procedure and continue with the linearization of the nonlinear weighted-residual expressions. Later, we develop the algebraic counterparts of the weighted-residual expressions and their linearized terms. Finally, in Section 6, we perform representative numerical examples that fit a set of novel experimental data obtained from both uniaxial extension and simple shear tests in a quasi-static manner.

2. Multi-field problem for failure in anisotropic continuum

In this section, we focus on the primary field variables, namely the crack phase-field d and the deformation map $\boldsymbol{\varphi}$ governed by the Euler–Lagrange equations which determine the diffusive crack topology and the balance of linear momentum. We introduce the finite elasticity in anisotropic solids paying attention to the structure of the tissue. Next we briefly motivate the crack phase-field in a one-dimensional setting and continue with the modeling of failure in three-dimensional continua which resorts to [47,44].

2.1. The primary field variables of the multi-field problem

Let us assume a material body at time $t_0 \in \mathcal{T} \subset \mathbb{R}$, which we refer to as the reference configuration in the three-dimensional space designated by $\mathcal{B} \subset \mathbb{R}^3$ with the material point $\boldsymbol{X} \in \mathcal{B}$. In the same manner the placement of the deformed body at current time $t \in \mathcal{T} \subset \mathbb{R}$ we refer to as the spatial configuration denoted by $\mathcal{S} \subset \mathbb{R}^3$ with the spatial point $\boldsymbol{x} \in \mathcal{S}$ mapped through the deformation map $\boldsymbol{\varphi}$, see Fig. 2. As long as $t \subset \mathbb{R}$ is fixed, one can also write $\boldsymbol{\varphi}_t(\boldsymbol{X})$ [49]. Its definition renders

$$\boldsymbol{\varphi}_t(\boldsymbol{X}) : \begin{cases} \mathcal{B} \times \mathcal{T} \rightarrow \mathcal{S}, \\ (\boldsymbol{X}, t) \mapsto \boldsymbol{x} = \boldsymbol{\varphi}(\boldsymbol{X}, t). \end{cases} \tag{1}$$

Additionally let us introduce the surface $\partial \mathcal{B} \subset \mathbb{R}^2$ of the reference configuration $\mathcal{B} \subset \mathbb{R}^3$. Alongside with the deformation map $\boldsymbol{\varphi}$ in (1) we now elucidate the basic geometric mapping for the crack phase-field d. The time-dependent auxiliary crack phase-field parameter is

$$d : \begin{cases} \mathcal{B} \times \mathcal{T} \rightarrow [0, 1], \\ (\boldsymbol{X}, t) \mapsto d(\boldsymbol{X}, t), \end{cases} \tag{2}$$

which interpolates between the intact ($d = 0$) and the ruptured ($d = 1$) state of the material.

2.1.1. Kinematics

The material gradient of the deformation map $\boldsymbol{\varphi}$ leads to the deformation gradient

$$\boldsymbol{F} = \nabla \boldsymbol{\varphi}, \tag{3}$$

which maps the unit Lagrangian line element $\mathrm{d}\boldsymbol{X}$ onto its Eulerian counterpart $\mathrm{d}\boldsymbol{x} = \boldsymbol{F}\mathrm{d}\boldsymbol{X}$. The gradient operators $\nabla[\bullet]$ and $\nabla_x[\bullet]$ denote the gradient operator with respect to the reference $\boldsymbol{X}$ and the spatial $\boldsymbol{x}$ coordinates, respectively. Moreover, the Jacobian $J := \det \boldsymbol{F} > 0$ characterizes the volume map of infinitesimal reference volume elements onto

associated spatial volume elements. Furthermore, we equip the two manifolds $\mathcal{B}$ and $\mathcal{S}$ with the covariant reference metric tensor $\boldsymbol{G}$ and spatial metric tensor $\boldsymbol{g}$. They are required for mapping between the co- and contravariant objects in the Lagrangian and Eulerian manifolds [49]. Then, the right and left Cauchy–Green tensors read

$$\boldsymbol{C} = \boldsymbol{F}^T \boldsymbol{g} \boldsymbol{F}, \qquad \boldsymbol{b} = \boldsymbol{F} \boldsymbol{G}^{-1} \boldsymbol{F}^T, \tag{4}$$

which measure the deformation in the Lagrangian and Eulerian configurations, respectively. The energy stored in a hyperelastic isotropic material is characterized by the invariants

$$I_1 = \text{tr} \boldsymbol{C}, \qquad I_2 = \frac{1}{2} \left[I_1^2 - tr(\boldsymbol{C}^2) \right], \qquad I_3 = \det \boldsymbol{C}. \tag{5}$$

The anisotropic response of biological tissues requires the description of additional invariants. To this end, we introduce two reference unit vectors $\boldsymbol{M}$ and $\boldsymbol{M}'$ for the fiber orientations and their spatial counterparts

$$\boldsymbol{m} = \boldsymbol{F} \boldsymbol{M}, \qquad \boldsymbol{m}' = \boldsymbol{F} \boldsymbol{M}', \tag{6}$$

which idealize the micro-structure of the arterial wall. We can express the related Eulerian form of the structure tensors $\boldsymbol{A_m}$ and $\boldsymbol{A_{m'}}$ as follows

$$\boldsymbol{A_m} = \boldsymbol{m} \otimes \boldsymbol{m}, \qquad \boldsymbol{A_{m'}} = \boldsymbol{m}' \otimes \boldsymbol{m}'. \tag{7}$$

Upon simplifications elucidated through a particular material response provided by experiments and the incompressibility condition, i.e. $I_3 = 1$, the only isotropic invariant remains to render the isotropic mechanical response of the tissue is I_1 which takes the following form in the spatial configuration

$$I_1 = \boldsymbol{g} : \boldsymbol{b}. \tag{8}$$

Besides, the physically meaningful additional invariants

$$I_4 = \boldsymbol{m} \cdot \boldsymbol{g} \boldsymbol{m}, \qquad I_6 = \boldsymbol{m}' \cdot \boldsymbol{g} \boldsymbol{m}' \tag{9}$$

are sufficient to capture the anisotropic response of the thoracic aortic tissue.

2.1.2. Finite elasticity of an anisotropic solid

Finite elasticity of biological tissues is governed by the balance equation derived from the principle of minimum potential energy, i.e.

$$\boldsymbol{\varphi} = \text{Arg} \left\{ \inf_{\boldsymbol{\varphi} \in \mathcal{W}_\varphi} E(\boldsymbol{\varphi}) - P(\boldsymbol{\varphi}) \right\}, \tag{10}$$

with the energy storage functional E and the external work functional P according to

$$E(\boldsymbol{\varphi}) = \int_\mathcal{B} \Psi(\boldsymbol{F}, \boldsymbol{A_m}, \boldsymbol{A_{m'}}) \mathrm{d}V, \qquad P(\boldsymbol{\varphi}) = \int_\mathcal{B} \rho_0 \bar{\boldsymbol{\gamma}} \cdot \boldsymbol{\varphi} \mathrm{d}V + \int_{\partial \mathcal{B}_t} \bar{\boldsymbol{T}} \cdot \boldsymbol{\varphi} \mathrm{d}A, \tag{11}$$

respectively. Therein ρ_0, $\bar{\boldsymbol{\gamma}}$ and $\bar{\boldsymbol{T}}$ are the density, the prescribed body force and the surface traction in the reference configuration, respectively, while Ψ denotes the free-energy function per unit reference volume; the specific form for the constitutive behavior of arterial walls is introduced in Section 4.1. The minimization problem (10) is subjected to Dirichlet-type boundary conditions, i.e.

$$\mathcal{W}_\varphi := \{ \boldsymbol{\varphi} \mid \boldsymbol{\varphi} \in H^1(\mathcal{B}), \ \boldsymbol{\varphi} = \bar{\boldsymbol{\varphi}} \text{ where } \bar{\boldsymbol{\varphi}} \in \partial \mathcal{B}_\varphi \}. \tag{12}$$

According to the minimization principle, the deformation map $\boldsymbol{\varphi}$ delineated by a respective field minimizes the functional (10) which leads to the balance equation

$$\text{Div} \, \boldsymbol{P} + \rho_0 \bar{\boldsymbol{\gamma}} = \boldsymbol{0} \tag{13}$$

for a quasi-static deformation in the domain $\mathcal{B}$ along with the Neumann-type boundary condition

$$\boldsymbol{P} \cdot \boldsymbol{N} = \bar{\boldsymbol{T}} \quad \text{on } \partial \mathcal{B}_t. \tag{14}$$
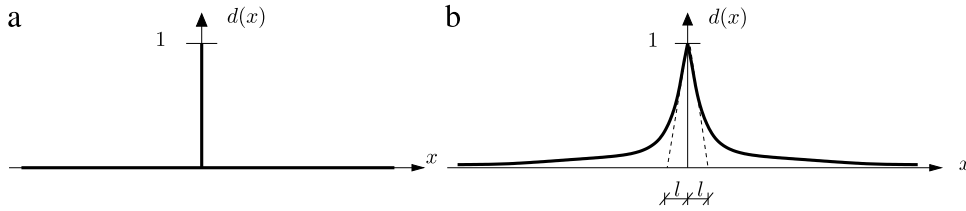
Fig. 3. (a) Sharp crack topology described by the Kronecker delta function $d(x) = \delta(x)$ for vanishing length-scale parameter $l \to 0$; (b) diffusive crack topology $d(x) = e^{-|x|/l}$ with a length-scale parameter equal to l.
Source: Adopted from [44].

The balance equation (13) is the Euler–Lagrange equation of the minimization problem (10). Herein, $\boldsymbol{P}$ is the first Piola–Kirchhoff stress tensor and $\boldsymbol{N}$ is the Lagrangian unit surface normal vector.

2.2. Ginzburg–Landau type phase-field model for diffusive cracks

In this section, the Ginzburg–Landau type phase-field approach for brittle fracture of isotropic solids will be briefly summarized, as outlined in [47,44]. The extension of the brittle fracture to the anisotropic solid will be provided in Section 3.

2.2.1. Field equation for crack phase-field in one-dimensional setting

In order to motivate the phase-field approximation to cracking phenomenon, an infinite one-dimensional bar $L = [-\infty, +\infty]$ with a crack that initiates at the origin $x = 0$ can be contemplated. The domain is then defined to be $\mathcal{B} = \Gamma \times L$ with a constant cross-section Γ on $x \in L$. The assisting crack phase-field variable $d(x) \in [0, 1]$ characterizes the acute crack topology with

$$d(x) := \delta(x) : \begin{cases} 1 & \text{for } x = 0, \\ 0 & \text{otherwise,} \end{cases} \tag{15}$$

described by the Kronecker delta function $\delta(x)$ as the discrete version of the Dirac delta function, where $d = 0$ and $d = 1$ mark the intact and the cracked (ruptured) state of the considered material, respectively, as depicted in Fig. 3(a). The auxiliary scalar field variable d represents the homogenized growth of micro-cracks and micro-voids within the material, as described in CDM. Next, this sharp crack topology is approximated to a diffusive crack topology via the exponential function

$$d(x) = e^{-|x|/l}, \tag{16}$$

which makes the crack spread over the axial domain L, with the length-scale parameter l regularizing the sharp crack topology, see Fig. 3(b). Note that Eq. (16) is the solution of the homogeneous ordinary differential equation

$$d(x) - l^2 d''(x) = 0 \tag{17}$$

subjected to the Dirichlet-type boundary conditions

$$d(0) = 1, \qquad d(\pm\infty) = 0. \tag{18}$$

From a purely mathematical standpoint the differential equation (17) can be regarded as the Euler–Lagrange equation of the variational principle

$$d = \text{Arg} \left\{ \inf_{d \in \mathcal{W}_d} I(d) \right\}, \tag{19}$$

with the space of admissible solutions $\mathcal{W}_d := \{d \,|\, d(0) = 1, \ d(\pm\infty) = 0\}$. The equivalent functional form delineating a potential for the one-dimensional problem is given as

$$I(d) = \frac{1}{2} \int_{\mathcal{B}} (d^2 + l^2 d'^2) \mathrm{d}x. \tag{20}$$

An integration of the Galerkin-type weak form of the differential equation (17) provides this functional.

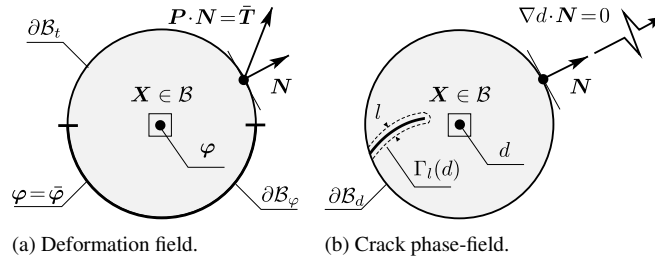(a) Deformation field.   (b) Crack phase-field.

Fig. 4. The multi-field problem: (a) mechanical problem of deformation; (b) evolution of the crack phase-field problem.

2.2.2. Field equation for crack phase-field in three-dimensional setting

The multi-dimensional formulation of the cracking in solid structures can be achieved in a similar way to the aforementioned one-dimensional motivation in Section 2.2.1. The respective deformation field is displayed in Fig. 4(a). For a non-deformable domain, the gradient operator can simply be taken as $\nabla_x[\bullet] = \nabla[\bullet]$. Provided that an acute crack surface topology at time t is given as $\Gamma(t) \subset \mathbb{R}^2$ in the solid $\mathcal{B}$, the regularized crack surface $\Gamma_l(d)$, see Fig. 4(b), adopts the following multi-dimensional form

$$\Gamma_l(d) = \int_{\mathcal{B}} \gamma(d, \nabla d)\mathrm{d}V, \tag{21}$$

where the volume-specific crack surface reads

$$\gamma(d, \nabla d) = \frac{1}{2l}(d^2 + l^2|\nabla d|^2). \tag{22}$$

Following the steps employed in the one-dimensional problem, we can now state the minimization principle

$$d(\boldsymbol{X}, t) = \mathrm{Arg} \left\{ \inf_{d \in \mathcal{W}_{\Gamma(t)}} \Gamma_l(d) \right\}, \tag{23}$$

along with the Dirichlet-type boundary constraint

$$\mathcal{W}_{\Gamma(t)} = \{d | d(\boldsymbol{X}, t) = 1 \text{ at } \boldsymbol{X} \in \Gamma(t)\}. \tag{24}$$

Upon the minimization of the regularized crack surface functional we derive the Euler–Lagrange equations of the above stated variational principle, i.e.

$$d - l^2 \Delta d = 0 \quad \text{in } \mathcal{B} \quad \text{and} \quad \nabla d \cdot \boldsymbol{N} = 0 \quad \text{on } \partial \mathcal{B}, \tag{25}$$

where Δd signifies the Laplacian of the crack phase-field which interpolates between the intact and the ruptured state of the material proportional to the length-scale parameter l, as depicted in Fig. 4(b), and $\boldsymbol{N}$ is the unit surface normal oriented outward in the reference configuration. The Euler–Lagrange equations (25) are derived in the Appendix, see also [45].

3. Governing equations of the multi-field problem

Now we are focusing on the minimization principle of the global power balance that governs the multi-field problem, which yields the coupled balance equations for the evolution of the crack phase-field and the balance of linear momentum.

3.1. Energy storage functional in an anisotropic solid

As a point of departure, we redefine the energy storage functional $(11)_1$ for the hyperelasticity of an anisotropic solid as

$$E(\boldsymbol{\varphi}, d) := \int_{\mathcal{B}} \Psi(\boldsymbol{F}, \boldsymbol{A_m}, \boldsymbol{A_{m'}}; d)\mathrm{d}V \tag{26}$$

in terms of the free-energy function Ψ for a degrading continuum, with

$$\Psi(\boldsymbol{F}, \boldsymbol{A_m}, \boldsymbol{A_{m'}}; d) := g(d)\, \Psi_0(\boldsymbol{F}, \boldsymbol{A_m}, \boldsymbol{A_{m'}}), \tag{27}$$

where Ψ_0 is the effective free-energy function of the hypothetical intact solid. A monotonically decreasing quadratic degradation function, i.e.

$$g(d) := (1 - d)^2, \tag{28}$$

describes the degradation of the solid with the evolving crack phase-field parameter d, with the following growth conditions:

$$g'(d) \leq 0 \quad \text{with } g(0) = 1, \; g(1) = 0, \; g'(1) = 0. \tag{29}$$

The first condition ensures degradation, while the second and third conditions set the limits for the intact and the ruptured state, and the final condition ensures the saturation at $d \to 1$.

3.2. Rate of energy storage functional and external power functional

Time derivative of (26) gives the rate of energy storage functional

$$\mathcal{E}(\dot{\boldsymbol{\varphi}}, \dot{d}; \boldsymbol{\varphi}, d) := \int_{\mathcal{B}} (\boldsymbol{P} : \dot{\boldsymbol{F}} - f\dot{d})\mathrm{d}V. \tag{30}$$

Herein,

$$\boldsymbol{P} = \partial_{\boldsymbol{F}}\, \Psi(\boldsymbol{F}, \boldsymbol{A_m}, \boldsymbol{A_{m'}}; d), \qquad f := -\partial_d\, \Psi(\boldsymbol{F}, \boldsymbol{A_m}, \boldsymbol{A_{m'}}; d) \tag{31}$$

are the first Piola–Kirchhoff stress tensor $\boldsymbol{P}$ and the energetic force f which is work conjugate to the crack phase-field d, respectively. The external power functional can be described as

$$\mathcal{P}(\dot{\boldsymbol{\varphi}}) = \int_{\mathcal{B}} \rho_0 \bar{\boldsymbol{\gamma}} \cdot \dot{\boldsymbol{\varphi}}\,\mathrm{d}V + \int_{\partial\mathcal{B}_t} \bar{\boldsymbol{T}} \cdot \dot{\boldsymbol{\varphi}}\,\mathrm{d}A. \tag{32}$$

3.3. Crack energy functional and crack dissipation functional

The crack energy functional D_c can be defined with the help of the volume-specific crack surface (22) according to

$$D_c(d) = \int_{\mathcal{B}} g_c \gamma(d, \nabla d)\mathrm{d}V, \tag{33}$$

where g_c denotes the critical fracture energy required to convert an un-cracked matter into a cracked matter. The evolution of (33) yields the crack dissipation functional $\mathcal{D}$, i.e.

$$\mathcal{D}(\dot{d}) = \int_{\mathcal{B}} g_c[\delta_d \gamma(d, \nabla d)]\dot{d}\,\mathrm{d}V, \tag{34}$$

where $\delta_d \gamma$ denotes the variational derivative of the volume-specific crack surface γ, [44], with the explicit form

$$\delta_d \gamma = \frac{1}{l}(d - l^2 \Delta d), \tag{35}$$

which can be shown in an analogous manner to that given in the Appendix. The second law of thermodynamics requires that the dissipation functional has to be non-negative for all admissible deformation processes, i.e. $\mathcal{D} \geq 0$.

3.4. Variational formulation based on power balance

The above stated functionals (30), (32) and (34) yield the power balance for the multi-field problem

$$\Pi(\dot{\boldsymbol{\varphi}}, \dot{d}) := \mathcal{E}(\dot{\boldsymbol{\varphi}}, \dot{d}) + \mathcal{D}(\dot{d}) - \mathcal{P}(\dot{\boldsymbol{\varphi}}) = 0. \tag{36}$$

On the basis of (36), a rate-type mixed variational principle can be constructed via a minimization principle for the quasi-static process, i.e.

$$\{\dot{\boldsymbol{\varphi}}, \dot{d}\} = \text{Arg} \left\{ \inf_{\dot{\boldsymbol{\varphi}} \in \mathcal{W}_\varphi} \inf_{\dot{d} \in \mathcal{W}_d} \Pi(\dot{\boldsymbol{\varphi}}, \dot{d}) \right\}, \tag{37}$$

with the admissible domains for the state variables

$$\begin{aligned} \mathcal{W}_\varphi &:= \{\dot{\boldsymbol{\varphi}} \mid \dot{\boldsymbol{\varphi}} = \mathbf{0} \text{ on } \partial \mathcal{B}_\varphi\}, \\ \mathcal{W}_d &:= \{\dot{d} \mid \dot{d} = 0 \text{ on } \partial \mathcal{B}_d\}. \end{aligned} \tag{38}$$

The variation of the functional leads to the Euler–Lagrange equations which describe the multi-field problem for the brittle fracture of an anisotropic hyperelastic solid, i.e.

$$\begin{aligned} &1: \text{Div}\, \boldsymbol{P} + \rho_0 \bar{\boldsymbol{\gamma}} = \mathbf{0}, \\ &2: (f - g_c \delta_d \gamma)\dot{d} = 0, \end{aligned} \tag{39}$$

along with the loading–unloading conditions ensuring the principal of maximum dissipation during an evolution of the crack phase-field parameter d, i.e.

$$\dot{d} \geq 0, \qquad f - g_c \delta_d \gamma \leq 0, \qquad (f - g_c \delta_d \gamma)\dot{d} = 0. \tag{40}$$

The first condition ensures the irreversibility of the evolution of the crack phase-field parameter. The second condition is an equality for an evolving crack, and it is negative for a stable crack. The third condition is the balance law for the evolution of the crack phase-field subject to the former conditions. The balance of static equilibrium (39)$_1$ can be recast, by making use of the Piola identity, into the following form

$$J \text{div}\, (J^{-1} \boldsymbol{\tau}) + \rho_0 \bar{\boldsymbol{\gamma}} = \mathbf{0}, \tag{41}$$

where $\boldsymbol{\tau}$ denotes the Kirchhoff stress tensor.

4. Constitutive equations of the multi-field problem

In this section, we shed light on (i) the constitutive equations that capture the nonlinear anisotropic response of arterial tissues, and (ii) the associated energy-based anisotropic failure criterion that portrays the state of the material at which the cracking starts and propagates.

4.1. Constitutive equations

To characterize the local anisotropic mechanical response of an intact aortic tissue we specify the free-energy function Ψ_0 in (27) and adopt the polyconvex, invariant-based anisotropic free-energy function

$$\Psi_0(\boldsymbol{F}, \boldsymbol{A_m}, \boldsymbol{A_{m'}}) := \Psi_0^{\text{iso}}(J, I_1) + \Psi_0^{\text{ani}}(I_4, I_6), \tag{42}$$

which additively decomposes into an isotropic neo-Hookean part responsible for the mechanical behavior of the ground matrix, i.e.,

$$\Psi_0^{\text{iso}}(J, I_1) := \kappa(J - \ln J - 1) + \frac{\mu}{2}(I_1 - 2 \ln J - 3), \tag{43}$$

and an exponential anisotropic free-energy function taking into account the contributions of the collagen fibers, i.e. [1]

$$\Psi_0^{\text{ani}}(I_4, I_6) := \frac{k_1}{2k_2} \sum_{i=4,6} \{\exp[k_2(I_i - 1)^2] - 1\}, \tag{44}$$

idealized by two distinct families of collagen fibers. Therein, κ denotes the penalty parameter whereas μ is the shear modulus. In the anisotropic term k_1 and k_2 stand for a stress-like material parameter and a dimensionless parameter, respectively. In the free-energy function (42) the anisotropic terms in (44) only contribute when the fibers are extended, that is when $I_4 > 1$ or $I_6 > 1$. If one or more of these conditions is not satisfied then the relevant part of the anisotropic function is omitted from (44). If, e.g., I_4 and I_6 are less than or equal to 1, then the function Ψ_0 is purely isotropic.

At this point we briefly touch upon some aspects regarding the computational treatment of the incompressible material behavior. The studies [50,51] discuss the non-physical volumetric deformation of an anisotropic material for the case that the hyperelastic model stated in (42) is mistakenly used in the compressible domain; e.g., a sphere reinforced with one family of fibers would be deformed into a sphere with a larger size upon inflation instead of an ellipsoidal shape. Another study [52] mentions that the volumetric–deviatoric split gives rise to a non-physical reduction in the stress along the fiber direction lowered through the lateral expansion which leads to an increase in the volume ratio. A careful treatment of incompressible materials is necessary since very large values of the penalty parameter κ may lead to ill-conditioning of the global tangent arrays, known as locking. This can be circumvented by mixed finite element methods due to a three-field Hu–Washizu variational principle along with the augmented Lagrangian method to enforce incompressibility. For more details, we refer to, e.g., [53–55]. Another strategy is based on the use of higher-order elements which can eliminate the parasitic stresses, see [56]. The use of mixed element formulations, however, requires special attention, particularly in phase-field problems of fracture since the degradation of the uniform volumetric response within an element domain cannot be arbitrarily chosen, i.e. the phase-field d calculated at each Gauss point does not match with the volumetric response described on the element level. In the view of the aforementioned information and our main focus on modeling fracture we have tried to avoid such computational complexities at this stage and have chosen the penalty parameter κ to be $\approx 10^3 \mu$ which allows the analysis of a nearly incompressible material (compressibility effects are small).

Exploiting the Coleman–Noll procedure on the Clausius–Planck inequality, and using the form of the free-energy function Ψ as introduced in (27), we may retrieve the Kirchhoff stress tensor $\boldsymbol{\tau}$ as follows

$$\boldsymbol{\tau} := 2\partial_{\boldsymbol{g}} \Psi = g(d)\boldsymbol{\tau}_0, \quad \boldsymbol{\tau}_0 = 2\partial_{\boldsymbol{g}} \Psi_0, \tag{45}$$

where $g(d)$ is the monotonically decreasing quadratic degradation function as provided in (28). Insertion of (42) along with (43) and (44) into the definition (45)$_2$ leads to the stress expression for the intact material

$$\boldsymbol{\tau}_0 = \hat{p}\boldsymbol{g}^{-1} + 2\mu(\boldsymbol{b} - \boldsymbol{g}^{-1}) + 2\psi_4 \boldsymbol{m} \otimes \boldsymbol{m} + 2\psi_6 \boldsymbol{m}' \otimes \boldsymbol{m}', \tag{46}$$

where $\hat{p} := \kappa(J - 1)$, and the deformation-dependent scalar coefficients ψ_4 and ψ_6 are defined as

$$\begin{aligned} \psi_4 &:= \partial_{I_4} \Psi_0 = k_1(I_4 - 1) \exp[k_2(I_4 - 1)^2], \\ \psi_6 &:= \partial_{I_6} \Psi_0 = k_1(I_6 - 1) \exp[k_2(I_4 - 1)^2]. \end{aligned} \tag{47}$$

Furthermore we need to derive the Kirchhoff stress tensor $\boldsymbol{\tau}$ with respect to the Eulerian metric $\boldsymbol{g}$ to obtain the following Eulerian elasticity tensors

$$\mathbb{C} := 4\partial^2_{\boldsymbol{gg}} \Psi = g(d)\mathbb{C}_0, \quad \mathbb{C}_0 = 4\partial^2_{\boldsymbol{gg}} \Psi_0. \tag{48}$$

Insertion of (46) and (47) into the definition (48)$_2$ gives the Eulerian elasticity tensor $\mathbb{C}_0$ for the intact material

$$\mathbb{C}_0 = (\hat{p} + \kappa)\boldsymbol{g}^{-1} \otimes \boldsymbol{g}^{-1} - 2\hat{p}\mathbb{I}_{\boldsymbol{g}^{-1}} + 2\mu \mathbb{I}_{\boldsymbol{g}^{-1}} + 4\psi_{44}\mathbb{M} + 4\psi_{66}\mathbb{M}', \tag{49}$$

where the symmetric fourth-order identity tensor $\mathbb{I}_{\boldsymbol{g}^{-1}}$ has the following index representation: $\mathbb{I}^{ijkl} = (g^{ik}g^{jl} + g^{il}g^{jk})/2$ which is with respect to the metric $\boldsymbol{g}^{-1}$. In addition, the scalar coefficients ψ_{44} and ψ_{66} can be given as

$$\begin{aligned} \psi_{44} &:= \partial_{I_4}\psi_4 = k_1[1 + 2k_2(I_4 - 1)^2] \exp[k_2(I_4 - 1)^2], \\ \psi_{66} &:= \partial_{I_6}\psi_6 = k_1[1 + 2k_2(I_6 - 1)^2] \exp[k_2(I_6 - 1)^2], \end{aligned} \tag{50}$$

and the fourth-order structure tensors take on the following form

$$\mathbb{M} := \boldsymbol{m} \otimes \boldsymbol{m} \otimes \boldsymbol{m} \otimes \boldsymbol{m}, \qquad \mathbb{M}' := \boldsymbol{m}' \otimes \boldsymbol{m}' \otimes \boldsymbol{m}' \otimes \boldsymbol{m}'. \tag{51}$$

4.2. Energy-based anisotropic failure criterion

According to experimental data of aortic tissues the related failure mechanism is anisotropic, see, e.g., [57,48]. In order to describe the anisotropic failure, we further elaborate on the equation for the evolution of the crack phase-field and substitute the Eqs. (31)$_2$, (35) in (39)$_2$ for $\dot{d} \geq 0$ and then (27), (28) in (31)$_2$ to obtain the following

$$f - \frac{g_c}{l}(d - l^2 \Delta d) = 0, \quad f = 2(1-d)\Psi_0. \tag{52}$$

We now assume distinct failure processes for the ground matrix and the fibers. Accordingly, the energetic force f can be additively decomposed into an isotropic part f_{iso} and an anisotropic part f_{ani} according to

$$f = f_{\text{iso}} + f_{\text{ani}} \begin{cases} f_{\text{iso}} = 2(1-d)\,\Psi_0^{\text{iso}}, \\ f_{\text{ani}} = 2(1-d)\,\Psi_0^{\text{ani}}. \end{cases} \tag{53}$$

Next, we introduce the distinct critical fracture energies over length scale g_c^{iso}/l for the ground matrix and g_c^{ani}/l for the fibers which are dual to the free-energy functions for the isotropic and the anisotropic parts, respectively, see (42). Consequently, (52) can be modified to account for the distinct failure assumption. After some simple algebraic manipulations, we obtain

$$2(1-d)\frac{\Psi_0^{\text{iso}}}{g_c^{\text{iso}}/l} = d - l^2 \Delta d, \qquad 2(1-d)\frac{\Psi_0^{\text{ani}}}{g_c^{\text{ani}}/l} = d - l^2 \Delta d. \tag{54}$$

In the subsequent treatment we define dimensionless crack driving functions for the isotropic ($\bar{\mathcal{H}}^{\text{iso}}$) and anisotropic ($\bar{\mathcal{H}}^{\text{ani}}$) parts in (54), i.e.

$$\bar{\mathcal{H}}^{\text{iso}} = \frac{\Psi_0^{\text{iso}}}{g_c^{\text{iso}}/l}, \qquad \bar{\mathcal{H}}^{\text{ani}} = \frac{\Psi_0^{\text{ani}}}{g_c^{\text{ani}}/l}. \tag{55}$$

By superposing the isotropic and anisotropic failure processes (54), we obtain with the use of (55)

$$d - l^2 \Delta d = (1-d)\bar{\mathcal{H}}, \quad \text{where } \bar{\mathcal{H}} = \bar{\mathcal{H}}^{\text{iso}} + \bar{\mathcal{H}}^{\text{ani}}. \tag{56}$$

The left-hand side of (56)$_1$ is the geometric resistance to crack growth whereas the right-hand side is the local source term for crack growth [27]. In order to enforce the irreversibility condition and prevent the healing effects, the dimensionless source term (56)$_2$ is modified, i.e.

$$\mathcal{H}(t) = \max_{s \in [0,t]} \left[\langle \bar{\mathcal{H}}(s) - 1 \rangle \right]. \tag{57}$$

In the above, the Macaulay brackets $\langle (\bullet) \rangle = [(\bullet) + |(\bullet)|]/2$ filter out the positive values for $\bar{\mathcal{H}}(s)$ and keeps the anisotropic solid intact below a threshold energy density, i.e. until the failure surface is reached. Hence, the crack phase-field does not evolve for a dimensionless crack source term $\bar{\mathcal{H}}(s) < 1$. The specific choice for $\mathcal{H}(t)$ in (57) ensures irreversibility of the crack evolution and a positive energetic force f. The failure Ansatz (57) can be used for transversely isotropic as well as anisotropic biological tissues with two or more fiber families including dispersion. In Section 6.1 we investigate some aspects of the proposed failure criterion for a simple homogeneous case.

5. Finite element formulation

In this section, we present a staggered set of algebraic equations derived from the strong forms of the coupled set of equations through a Galerkin type finite element formulation. At the first stage, we consider two decoupled sub-problems by the virtue of a one-pass operator-splitting. In the sequel, we construct the weak forms of the Eqs. (41), (39)$_2$ and consistently linearize them along the field variables, namely the deformation map $\boldsymbol{\varphi}(\boldsymbol{X}, t)$, the crack phase-field $d(\boldsymbol{X}, t)$. An identical temporal as well as spatial discretization scheme is employed for the deformation map and the crack phase-field. The field variables are appropriately discretized with isoparametric shape functions to transform the continuous integral equations of the nonlinear weighted-residuals and their linearizations to a set of coupled,

discrete algebraic equations. Finally, this set of algebraic equations are solved by a Newton-type iterative solver for the nodal degrees of freedom.

5.1. One-pass operator-splitting algorithm

We consider a discrete time increment $\tau = t_{n+1} - t_n$ where t_{n+1} and t_n stand for the current and previous time steps, respectively. The operator-splitting algorithm is composed of two sub-algorithms, i.e.

$$ALGO_{CM} = ALGO_C \circ ALGO_M. \tag{58}$$

Here, such an algorithm yields a decoupling within the time interval and results in partitioned symmetric structures for the mechanical and crack-growth sub-problems. In fact, the operator-splitting algorithm converts the non-convex coupled problem into two convex sub-problems which are computationally more feasible than the monolithic scheme. Within this context, the algorithm of each sub-problem is obtained as follows

$$(M) : \begin{cases} J \operatorname{div}(J^{-1}\boldsymbol{\tau}) + \rho_0 \bar{\boldsymbol{\gamma}} = \mathbf{0}, \\ \dot{d} = 0, \end{cases} \quad \text{and} \quad (C) : \begin{cases} \dot{\boldsymbol{\varphi}} = \mathbf{0}, \\ d - l^2 \Delta d - (1-d)\mathcal{H} = 0. \end{cases} \tag{59}$$

The (first) algorithm (M) is the mechanical predictor step which is solved for the frozen crack phase-field parameter $d = d_n$, while the algorithm (C) is the crack evolution step for the frozen deformation map $\boldsymbol{\varphi} = \boldsymbol{\varphi}_n$.

5.2. Galerkin-type weak formulation

This section is devoted to the transformation of the coupled balance equations into their weak forms through a conventional Galerkin procedure. To this end, we introduce two test function fields $\delta\boldsymbol{\varphi}$ and δd, which satisfy the essential boundary conditions, according to

$$\begin{aligned} \delta\boldsymbol{\varphi} &\in \mathcal{W}_{\delta\varphi} := \{\delta\boldsymbol{\varphi} \mid \delta\boldsymbol{\varphi} = \mathbf{0} \text{ on } \bar{\boldsymbol{\varphi}} \in \partial\mathcal{B}_\varphi\}, \\ \delta d &\in \mathcal{W}_{\delta d} := \{\delta d \mid \delta d = 0 \text{ on } \boldsymbol{X} \in \Gamma(d)\}. \end{aligned} \tag{60}$$

The strong form of the Eqs. (59) are multiplied with the admissible test functions (60) and integrated over the domain $\mathcal{B}$ leading to the weak form for the static force balance and the evolution of the crack phase-field. Following the Galerkin procedure, the Gaussian integral and the Cauchy theorems lead to the subsequent weighted-residual expressions of the field variables for the static force balance, i.e.

$$G^\varphi = G^\varphi_{\text{int}}(\delta\boldsymbol{\varphi}, \boldsymbol{\varphi}, d) - G^\varphi_{\text{ext}}(\delta\boldsymbol{\varphi}) = 0 \begin{cases} G^\varphi_{\text{int}} = \int_\mathcal{B} \operatorname{sym}[\nabla_x(\delta\boldsymbol{\varphi})] : \boldsymbol{\tau} \, \mathrm{d}V, \\ G^\varphi_{\text{ext}} = \int_\mathcal{B} \delta\boldsymbol{\varphi} \cdot \rho_0 \bar{\boldsymbol{\gamma}} \, \mathrm{d}V + \int_{\partial\mathcal{B}} \delta\boldsymbol{\varphi} \cdot \bar{\boldsymbol{T}} \, \mathrm{d}A, \end{cases} \tag{61}$$

where the body force $\bar{\boldsymbol{\gamma}}$ and the surface traction $\bar{\boldsymbol{T}}$ are assumed to be prescribed. Using similar arguments, the weak forms of the phase-field problem can be elaborated as

$$G^d = G^d_{\text{int}}(\delta d, \boldsymbol{\varphi}, d) - G^d_{\text{ext}}(\delta d) = 0 \begin{cases} G^d_{\text{int}} = \int_\mathcal{B} \delta d[d - (1-d)\mathcal{H}] \mathrm{d}V + \int_\mathcal{B} \nabla(\delta d) \cdot l^2 \nabla d \, \mathrm{d}V, \\ G^d_{\text{ext}} = 0. \end{cases} \tag{62}$$

The geometric and the constitutive terms endow the weighted-residual expressions in (61) and (62) with nonlinearity; hence, a reliable and efficient solution of these equations entails a consistent linearization with regard to all quantities, i.e. $\boldsymbol{\varphi}$ and d associated with the nonlinear problem about $\boldsymbol{\varphi} = \tilde{\boldsymbol{\varphi}}$ and $d = \tilde{d}$:

$$\begin{aligned} \operatorname{Lin}G^\varphi\big|_{\tilde{\boldsymbol{\varphi}}} &= G^\varphi(\delta\boldsymbol{\varphi}, \tilde{\boldsymbol{\varphi}}, d) + \Delta G^\varphi(\delta\boldsymbol{\varphi}, \tilde{\boldsymbol{\varphi}}, d; \Delta\boldsymbol{\varphi}) = 0, \\ \operatorname{Lin}G^d\big|_{\tilde{d}} &= G^d(\delta d, \boldsymbol{\varphi}, \tilde{d}) + \Delta G^d(\delta d, \boldsymbol{\varphi}, \tilde{d}; \Delta d) = 0. \end{aligned} \tag{63}$$

The above expressions are fashioned by Taylor's expansion through the Gâteaux derivative that yields the linear incremental terms ΔG^φ and ΔG^d, which are decomposed in the following way

$$\Delta G^\varphi = \Delta G^\varphi_{\text{int}} - \Delta G^\varphi_{\text{ext}}, \qquad \Delta G^d = \Delta G^d_{\text{int}} - \Delta G^d_{\text{ext}}. \tag{64}$$

Since we have prescribed values for the body force $\bar{\boldsymbol{\gamma}}$ and the surface traction $\bar{\boldsymbol{T}}$, the external increment vanishes, i.e. $\Delta G^\varphi_{\text{ext}} = 0$. Besides, we conclude that the external term ΔG^d_{ext} disappears as well. Accordingly, we first operate on $\Delta G^\varphi_{\text{int}}$ which takes on the following form

$$\Delta G^\varphi_{\text{int}} = \int_{\mathcal{B}} \{\text{sym}[\nabla_x(\delta\boldsymbol{\varphi})] : \mathbb{C} : \text{sym}[\nabla_x(\Delta\boldsymbol{\varphi})] + \nabla_x(\delta\boldsymbol{\varphi}) : \nabla_x(\Delta\boldsymbol{\varphi})\boldsymbol{\tau}\}\mathrm{d}V. \tag{65}$$

Maintaining the same formalism, we can now expand on the internal increment ΔG^d_{int} describing the linearization of the crack phase-field around $\tilde{d}$ at an incremental time step τ, i.e.

$$\Delta G^d_{\text{int}} = \int_{\mathcal{B}} \delta d(1 + \mathcal{H})\Delta d \, \mathrm{d}V + \int_{\mathcal{B}} \nabla(\delta d) \cdot l^2 \nabla(\Delta d) \, \mathrm{d}V. \tag{66}$$

5.3. Spatial discretization

We perform a spatial discretization of the field variables and construct residual vectors together with the element matrices. Here we briefly present an overview of the underlying theoretical aspects of the finite element discretization but mainly focus on the algebraic counterparts of the residual expressions. For an in-depth treatment of the discretization methods we refer to, e.g., [58,59]. Accordingly, we discretize the reference domain $\mathcal{B}$ into element sub-domains $\mathcal{B}^h_e$ within the body and the Neumann surface $\partial\mathcal{B}$ into $\partial\mathcal{B}^h_e$. Thus, we write

$$\mathcal{B} \approx \overset{n_{\text{el}}}{\underset{e=1}{\mathbf{A}}} \mathcal{B}^h_e, \qquad \partial\mathcal{B} \approx \overset{n^t_{\text{el}}}{\underset{e=1}{\mathbf{A}}} \partial\mathcal{B}^h_e, \tag{67}$$

where n_{el} is the number of finite elements while n^t_{el} stands for the number of surface finite elements. Then, the field variables $\boldsymbol{\varphi}$, d, the weighting functions $\delta\boldsymbol{\varphi}$, δd and the related increments $\Delta\boldsymbol{\varphi}$, Δd are interpolated by the Ansatz functions (shape functions) $\mathcal{N}$ in between physically meaningful free parameters, i.e. the values of the displacement and phase-field at the nodes. In fact, we discretize the field variables, the corresponding weighting functions and increments by means of the same $\mathcal{C}^0$ continuous shape functions (Bubnov–Galerkin method). These shape functions are then multiplied by the nodal values $\hat{\boldsymbol{x}}$, $\delta\hat{\boldsymbol{x}}$, and $\Delta\hat{\boldsymbol{x}}$ for the deformation field on each element. In an analogous manner, for each element the nodal values $\hat{d}$, $\delta\hat{d}$, and $\Delta\hat{d}$ of the crack phase-field are multiplied by the shape functions. In addition, we need the gradient of the weighting functions ($\nabla_x(\delta\boldsymbol{\varphi})$, $\nabla(\delta d)$) and the incremental fields ($\nabla_x(\Delta\boldsymbol{\varphi})$, $\nabla(\Delta d)$) to be obtained from the partial derivatives of the shape functions ($\nabla_x\mathcal{N}$, $\nabla\mathcal{N}$).

In the next step, we insert Eq. (67) and the aforestated expressions into (61) and (62), as formulated in Section 5.2, in order to obtain the discrete residual vectors

$$\mathbb{R}^\varphi = \overset{n_{\text{el}}}{\underset{e=1}{\mathbf{A}}} \sum_{i=1}^{n_{\text{en}}} \delta\hat{\boldsymbol{x}}^{\text{T}^i} \int_{\mathcal{B}^h_e} (\boldsymbol{B}^{\text{T}^i}\boldsymbol{\tau}_e - \mathcal{N}^i \rho_{0e}\bar{\boldsymbol{\gamma}}_e)\mathrm{d}V - \overset{n^t_{\text{el}}}{\underset{e=1}{\mathbf{A}}} \sum_{i=1}^{n_{\text{sf}}} \delta\hat{\boldsymbol{x}}^{\text{T}^i} \int_{\partial\mathcal{B}^h_e} \mathcal{N}^i \bar{\boldsymbol{T}}_e \mathrm{d}A = \boldsymbol{0},$$

$$\mathbb{R}^d = \overset{n_{\text{el}}}{\underset{e=1}{\mathbf{A}}} \sum_{i=1}^{n_{\text{en}}} \delta\hat{d}^i \int_{\mathcal{B}^h_e} \{\mathcal{N}^i[d_e - (1 - d_e)\mathcal{H}_e] + \nabla^{\text{T}}\mathcal{N}^i l_e^2 \nabla d_e\}\mathrm{d}V = 0, \tag{68}$$

where $(\bullet)_e$ denotes the matrix form of the associated quantities, e.g., $\boldsymbol{\tau}_e$ is the 6×1 Kirchhoff stress matrix, on a typical element, and n_{en} and n_{sf} denote the number of nodes per volume and surface element, respectively. In (68) we have also introduced the 6×3 matrix $\boldsymbol{B}^i$, associated with node i, which consists of the partial derivatives of the shape functions with respect to the spatial coordinates x_j. In the sequel, we identify the discrete forms of the linearized terms in analogy to the residual vectors by substituting the necessary arguments for the continuous representations in

Table 1
General solution algorithm for the multi-field problem in $[t_n, t_{n+1}]$.

1. *Initialization*	–	At time t_n given: deformation map, phase-field, history field $\boldsymbol{\varphi}_n, d_n, \mathcal{H}_n$
2. *Update*	–	Update the prescribed loads $\bar{\boldsymbol{\gamma}}, \bar{\boldsymbol{\varphi}}$ and $\bar{\boldsymbol{T}}$ at current time t_{n+1}
3. *Compute* $\boldsymbol{\varphi}_{n+1}$	–	Determine $\boldsymbol{\varphi}_{n+1}$ from the minimization problem of elasticity
$ALGO_M$	•	$G^\varphi = \int_{\mathcal{B}} \text{sym}[\nabla_x(\delta\boldsymbol{\varphi})] : \boldsymbol{\tau}\,\mathrm{d}V - \int_{\mathcal{B}} \delta\boldsymbol{\varphi} \cdot \rho_0 \bar{\boldsymbol{\gamma}}\,\mathrm{d}V - \int_{\partial\mathcal{B}} \delta\boldsymbol{\varphi} \cdot \bar{\boldsymbol{T}}\,\mathrm{d}A = 0$
4. *Compute history*	–	Check crack initiation/propagation condition, update history
	•	$\mathcal{H}(t_{n+1}) \leftarrow \begin{cases} \mathcal{H}(t_n) & \text{if}\quad \mathcal{H}(t_{n+1}) < \mathcal{H}(t_n) \\ \mathcal{H}(t_{n+1}) & \text{else} \end{cases}$
5. *Compute* d_{n+1}	–	Determine d_{n+1} from the minimization problem of crack topology
$ALGO_C$	•	$G^d = \int_{\mathcal{B}} \delta d[d - (1-d)\mathcal{H}]\mathrm{d}V + \int_{\mathcal{B}} \nabla(\delta d) \cdot l^2 \nabla d\,\mathrm{d}V = 0$

(65) and (66). The linearization process then reads

$$\text{Lin}\mathbb{R} = \mathbb{R} + \frac{\partial\mathbb{R}}{\partial\mathbb{U}}\Delta\mathbb{U}, \qquad \mathbb{R} = \begin{bmatrix} \mathbb{R}^\varphi \\ \mathbb{R}^d \end{bmatrix}, \qquad \mathbb{U} = \begin{bmatrix} \boldsymbol{\varphi}^h \\ d^h \end{bmatrix}. \tag{69}$$

The insertion of the discrete forms of the field variables yield the coupled element matrix. Thus,

$$\mathbb{K} = \frac{\partial\mathbb{R}}{\partial\mathbb{U}} = \begin{bmatrix} \mathbb{K}^{\varphi\varphi} & \mathbf{0} \\ \mathbf{0} & \mathbb{K}^{dd} \end{bmatrix}, \tag{70}$$

and the element matrices of each sub-problem take on the following forms

$$\begin{aligned}
\mathbb{K}^M &:= \mathbb{K}^{\varphi\varphi} = \overset{n_{\text{el}}}{\underset{e=1}{\mathbf{A}}} \sum_{i=1}^{n_{\text{en}}} \sum_{j=1}^{n_{\text{en}}} \delta\hat{\boldsymbol{x}}^{\mathrm{T}i} \boldsymbol{K}_{\varphi\varphi,e}^{ij} \Delta\hat{\boldsymbol{x}}^j, \\
\mathbb{K}^C &:= \mathbb{K}^{dd} = \overset{n_{\text{el}}}{\underset{e=1}{\mathbf{A}}} \sum_{i=1}^{n_{\text{en}}} \sum_{j=1}^{n_{\text{en}}} \delta\hat{d}^i \boldsymbol{K}_{dd,e}^{ij} \Delta\hat{d}^j,
\end{aligned} \tag{71}$$

where $\mathbb{K}^M$ is the stiffness matrix related to the mechanical predictor, while $\mathbb{K}^C$ is the stiffness matrix describing the crack evolution. The components of the tangent matrices $\boldsymbol{K}_{\varphi\varphi,e}^{ij}$ and $\boldsymbol{K}_{dd,e}^{ij}$ for one element related to the nodes i, j can be given as

$$\begin{aligned}
\boldsymbol{K}_{\varphi\varphi,e}^{ij} &= \int_{\mathcal{B}_e^h} (\boldsymbol{B}^{\mathrm{T}i} \boldsymbol{D}_e \boldsymbol{B}^j + \nabla_x^{\mathrm{T}} \mathcal{N}^i \boldsymbol{\tau}_e \nabla_x \mathcal{N}^j)\mathrm{d}V, \\
\boldsymbol{K}_{dd,e}^{ij} &= \int_{\mathcal{B}_e^h} [\mathcal{N}^i (1 + \mathcal{H}_e) \mathcal{N}^j + \nabla^{\mathrm{T}} \mathcal{N}^i l_e^2 \nabla \mathcal{N}^j]\mathrm{d}V,
\end{aligned} \tag{72}$$

where $\boldsymbol{D}_e$ designates the matrix form of the elasticity tensor $\mathbb{C}$ for a typical element. Table 1 summarizes the operator-splitting algorithm which forms the basis for the implementation of the numerical scheme in which the phase-field d is driven by the local history field $\mathcal{H}(t_{n+1})$.

6. Representative numerical examples

In this section, we illustrate the performance of the proposed crack phase-field model applied to aortic fracture through numerical simulations to capture the experimental data. The failure criterion with the related failure envelope is analyzed in Section 6.1 for a simple geometry and loading condition (homogeneous problem), while Sections 6.2 and 6.3 show numerical simulations for uniaxial extension and simple shear tests with the anisotropic failure criterion (57).

The experiments are conducted on aneurysmatic specimens extracted from the media of a human thoracic aorta possessing two families of collagen fibers. The performed numerical simulations are based on the experimental data
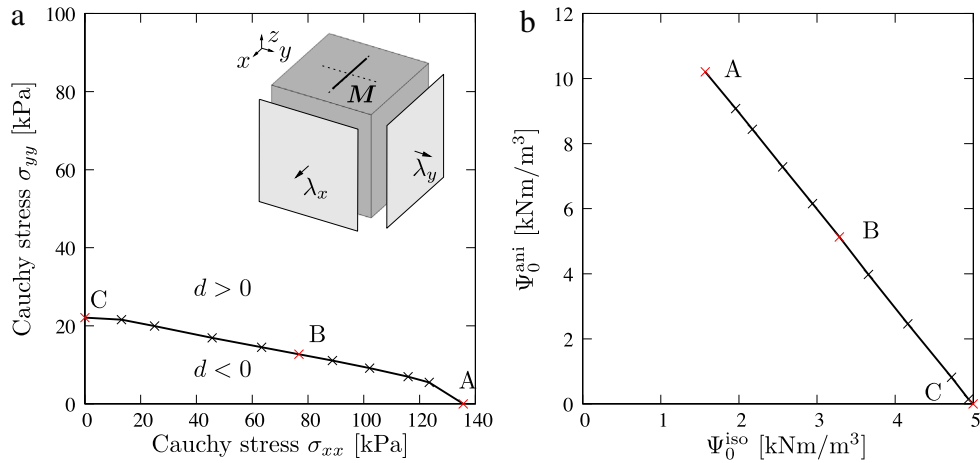
Fig. 5. (a) Unit cube with a transversely isotropic tissue consisting of one family of fibers with orientation $\boldsymbol{M}$ parallel to the x-direction — failure envelope in regard to the Cauchy stresses σ_{xx} and σ_{yy} at which the failure criterion is satisfied, leading to $d > 0$; (b) corresponding isotropic and anisotropic energy states of the tissue (Ψ_0^{iso}, Ψ_0^{ani}).

of the specimens which were obtained through different deformation modes (uniaxial extension and simple shear in the circumferential and longitudinal directions); for more details see the recent study [48], specimen *AVIII* therein.

6.1. Numerical investigation of the failure criterion for a homogeneous problem

Although the initiation and propagation of a crack in a tissue can become a highly inhomogeneous phenomenon in terms of stresses and strains, driven by an intricate combination of deformation modes, a homogeneous problem with simple loading conditions can provide further insight to the energy-based anisotropic failure criterion used in the present model. Therefore, we consider a unit cube discretized by one hexahedral element which resolves the analytical solution for the deformation and stress, and discards all non-local effects due to the gradient of the crack phase-field ∇d and the length-scale parameter l (=1 mm), see Fig. 5(a). In this case, the tissue is regarded to be transversely isotropic with one family of fibers oriented along the x-direction. The elastic parameters required for the constitutive law are chosen to be $\mu = 10$ kPa, $k_1 = 20$ kPa and $k_2 = 1$. As for the crack phase-field, the critical fracture energies are selected as $g_c^{\mathrm{iso}} = 5$ kPa mm and $g_c^{\mathrm{ani}} = 15$ kPa mm. We investigate several loading conditions. First, we perform uniaxial extension tests along the x and the y-direction with a stretch ratio $\lambda_x = 2$ and $\lambda_y = 2$, respectively. Subsequently, the tissue undergoes biaxial deformations with the stretch ratios λ_x:λ_y = 2:1.1, 2:1.25, 2:1.5, 2:1.75, 2:2, 1.75:2, 1.5:2, 1.25:2, and 1.1:2.

Fig. 5(a) demonstrates the obtained failure envelope at which the failure criterion is satisfied, leading to $d > 0$. The corresponding isotropic and anisotropic energy states of the tissue are shown in Fig. 5(b). Therein the uniaxial extension in the x-direction up to a stretch of 2 leads to a stress and energy state denoted by A, whereas C pinpoints the uniaxial extension in the y-direction up to a stretch of 2. The stress and energy states due to the equibiaxial stretch 2:2 are indicated by B. This study clearly addresses the anisotropy of the failure criterion. In fact, the plane-stress failure envelope exhibits an elliptic curve for the investigated stretch ratios, while the failure energy interpolates linearly between the anisotropic and isotropic free-energies for the transversely isotropic tissue.

6.2. Uniaxial extension tests of thoracic aorta with anisotropic failure

In the experimental investigations, excised aneurysmatic medial strips from a human thoracic aorta are tested along the circumferential (θ) and longitudinal (z) directions by means of uniaxial extension in accordance with the testing protocol documented in [48]. These aforecited tests are numerically reproduced *in silico* with a monotonic load pattern (stretch λ) exerted on the strips with an incision, as depicted in Fig. 6(a). The finite element mesh of the strip is generated with 3880 eight-node hexahedral elements with a length-scale parameter $l = 0.4$ mm. The generated mesh is refined in the regions between the incision and the opposite edge for which l satisfies $l \geq 2h$ for the crack zone to be
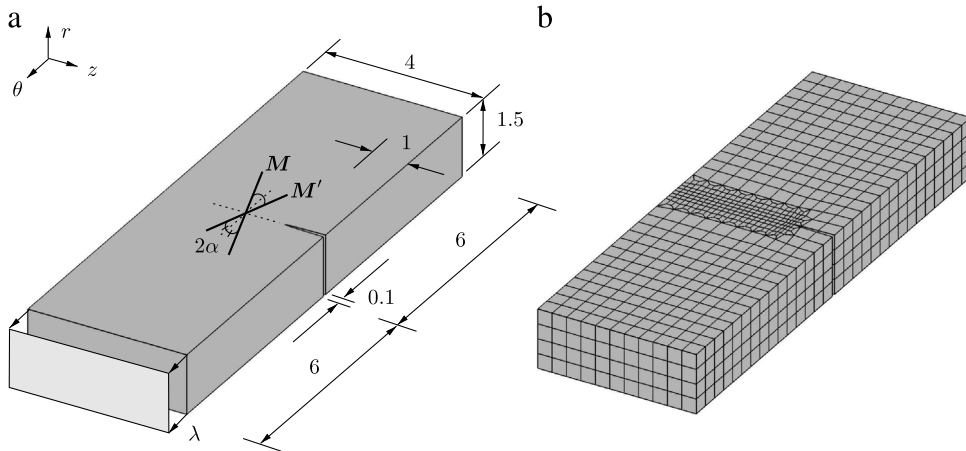
Fig. 6. (a) Geometry of the specimen oriented in the circumferential θ-direction, uniaxially loaded by stretch λ. The structure of the media is characterized by two families of fibers, oriented in the directions M and M' in the reference configuration, corresponding to the collagenous component of the material, and they are symmetrically arranged with respect to the cylinder axis — α is the angle between the fibers and the circumferential direction; (b) finite element mesh of the corresponding geometry with refinement around the incision. Dimensions are provided in millimeters.
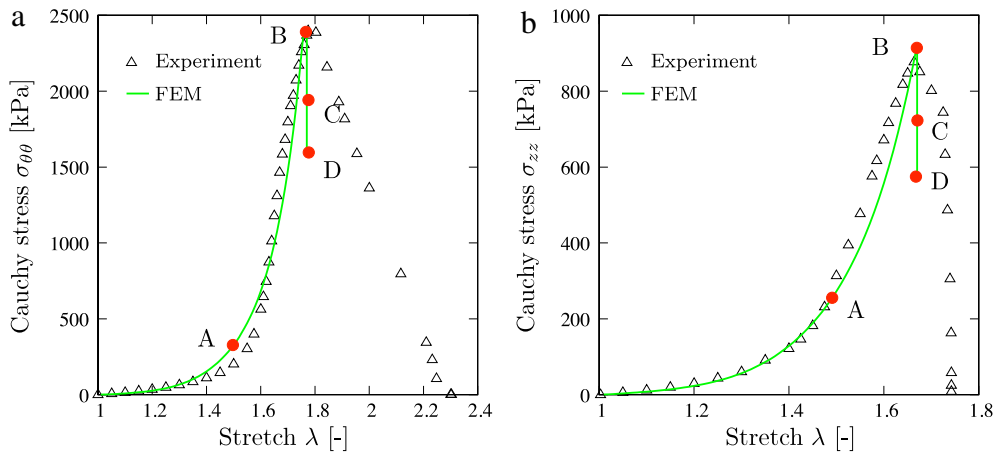
Fig. 7. Uniaxial extension test data (triangles) and corresponding finite element results (solid curves): Cauchy stress versus stretch for a strip in (a) the circumferential θ-direction and (b) the longitudinal z-direction.

resolved properly [44], where h denotes the minimum element size, see Fig. 6(b). The displacements are constrained at the $\theta = 0$, $r = 0$, and $z = 0$ planes along the θ-, r-, and z- directions, respectively. The geometry and the related finite element mesh of the incised strip extended along the longitudinal z- direction is the analogue of Fig. 6.

While the elastic material parameters are estimated via nonlinear least-squares analysis by utilizing *lsqnonlin* on MATLAB® at a material point, the critical fracture energies g_c^{iso} and g_c^{ani} according to (55) are identified for each test through a quantitative comparison of the stress–stretch curves of the simulation results with those of the corresponding experimental data. It should be noted that in the nonlinear least-squares analysis we used the stress–stretch data until the ultimate stress which leads to the aforementioned elastic material parameters. The elastic and the crack phase-field parameters are summarized in Table 2. For a comparison of uniaxial extension test data with the finite element results in terms of Cauchy stress versus stretch for strips in the circumferential and longitudinal directions see Fig. 7(a), (b). Note that the curves provided via finite element analysis are obtained by considering the average of all nodal stresses at the planes $\theta = 12$ mm and $z = 12$ mm in the circumferential and longitudinal directions, respectively. The results agree favorably with the anisotropic response of the tissue obtained from the experiments. The crack initiates from the tip of the incised region where the stress concentration and, therefore, the energy of the intact tissue takes on larger

Table 2
Elastic and crack phase-field parameters for anisotropic failure of aneurysmatic circumferential and longitudinal medial strips of an aorta under uniaxial extension.

Elastic	
	$\mu = 16.95$ kPa
	$k_1 = 243.57$ kPa
	$k_2 = 2.57$
	$\alpha = 44.5°$
Crack phase-field	
	$g_c^{iso} = 32$ kPa mm along the θ-direction
	$g_c^{ani} = 112$ kPa mm along the θ-direction
	$g_c^{iso} = 32$ kPa mm along the z-direction
	$g_c^{ani} = 35$ kPa mm along the z-direction
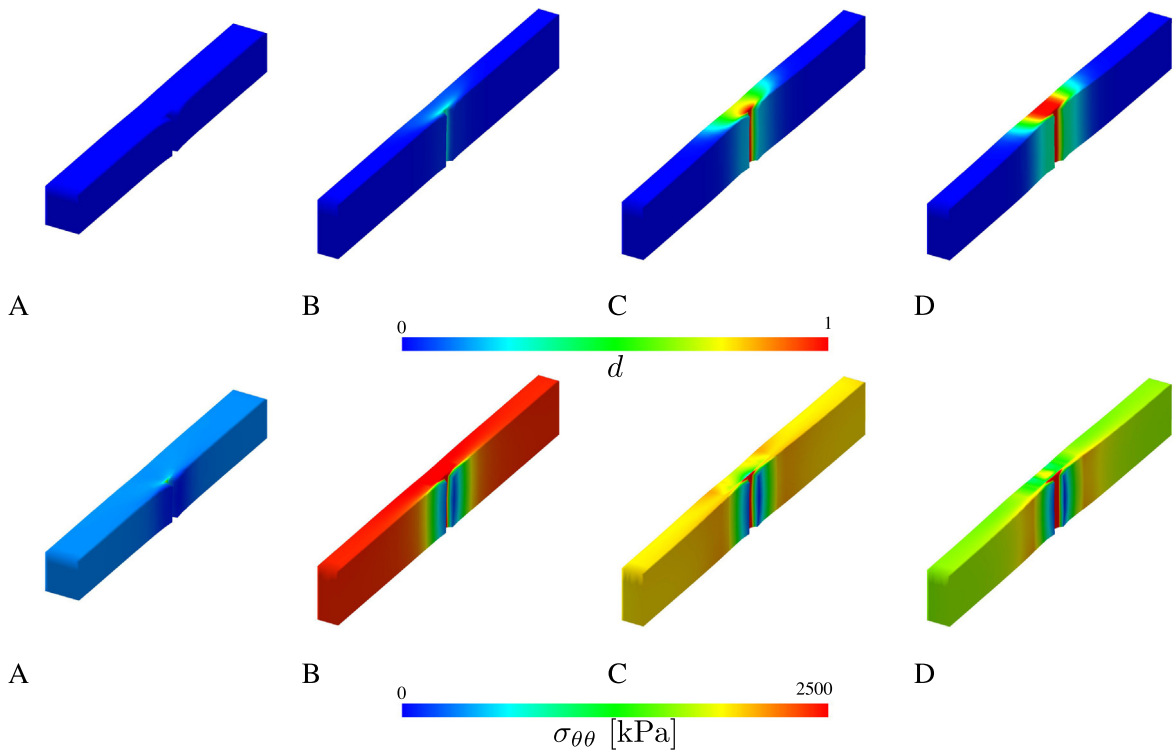
Fig. 8. Numerical results of uniaxial extension in the circumferential θ-direction with anisotropic failure at the stress–stretch locations A–D indicated in Fig. 7(a): (above) distribution of crack phase-field d; (below) corresponding circumferential Cauchy stress $\sigma_{\theta\theta}$.

values than the other regions, and hence satisfies the failure condition. What follows is a nearly straight pattern as the phase-field grows towards the opposite edge at which the failure occurs. This is realized by a sudden loss of the load-bearing capacity, as illustrated in the corresponding stress–stretch curves of Fig. 7. Fig. 8 shows the distributions of the crack phase-field d and the circumferential Cauchy stress $\sigma_{\theta\theta}$ at the particular stress–stretch locations A–D, as indicated in Fig. 7(a), while the related crack phase-field d and the longitudinal Cauchy stress σ_{zz} at the four states indicated in Fig. 7(b) are shown in Fig. 9.

6.3. Simple shear tests of thoracic aorta with anisotropic failure

Concerning the simple shear tests, the medial specimens are subjected to shear along the θ- and z-directions, referred to as $z\theta$ mode and θz mode (the first index refers to the plane while the second to the direction), respectively. Incisions are made to induce failure on a certain plane, see [48]. Such experiments are replicated computationally
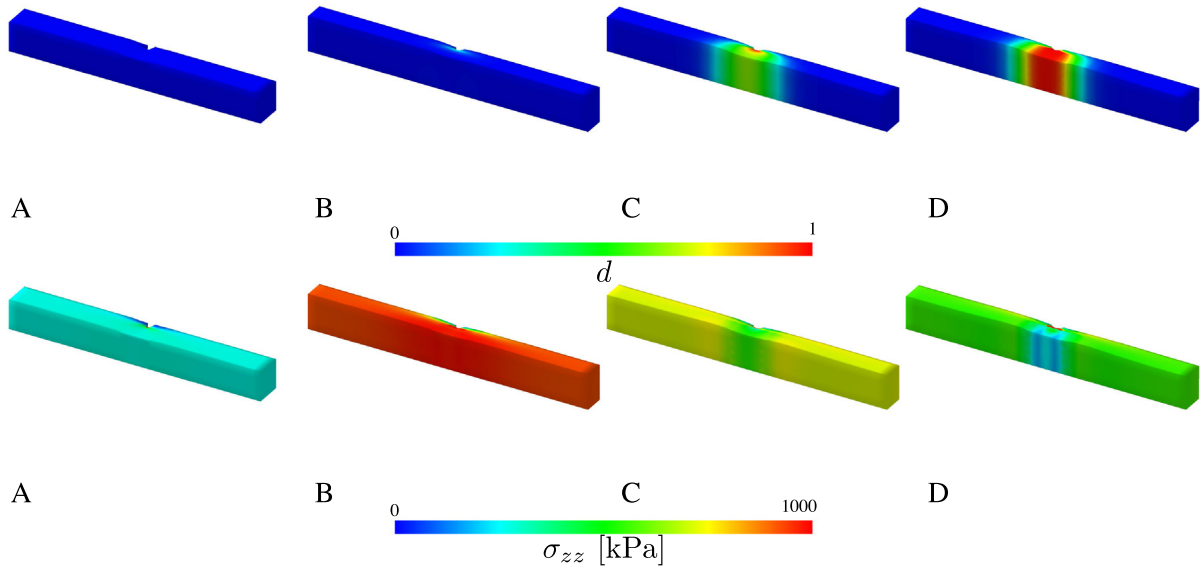
Fig. 9. Numerical results of uniaxial extension in the longitudinal z-direction with anisotropic failure at the stress–stretch locations A–D indicated in Fig. 7(b): (above) distribution of crack phase-field d; (below) corresponding longitudinal Cauchy stress σ_{zz}.

Table 3
Elastic and crack phase-field parameters for anisotropic failure of aneurysmatic aortic specimens under simple shear along the circumferential (θ) and longitudinal (z) directions.

Elastic	$\mu = 80.74$ kPa
	$k_1 = 62.04$ kPa
	$k_2 = 0.23$
	$\alpha = 53.68°$
Crack phase-field	$g_c^{\mathrm{iso}} = 80$ kPa mm along the θ-direction
	$g_c^{\mathrm{ani}} = 105$ kPa mm along the θ-direction
	$g_c^{\mathrm{iso}} = 120$ kPa mm along the z-direction
	$g_c^{\mathrm{ani}} = 240$ kPa mm along the z-direction

with respect to a monotonic shear load applied to the specimens with symmetric incisions; for the related geometries see Fig. 10(a), (c). In the sequel, the geometry of the specimen, which is sheared along the θ-direction ($z\theta$ mode), is discretized with 23 525 four-node tetrahedral elements with a length-scale parameter $l = 0.167$ mm, see Fig. 10(b), while for the other geometry (θz mode) 22 657 finite elements are used with $l = 0.25$ mm, see Fig. 10(d). Note that l is chosen to satisfy $l > 2h$ in order to resolve the crack surface properly, see [44]. The meshes are refined in the areas where the crack is expected to propagate in order to resolve the crack zone. With respect to the Dirichlet-boundary conditions the nodes on the $z = 0$ plane are constrained in three directions for the $z\theta$ mode, while those located on the $\theta = 0$ plane are constrained in three directions for the θz mode. The elastic material parameters are estimated via nonlinear least-squares analysis by utilizing *lsqnonlin* on MATLAB®. The critical fracture energies g_c^{iso} and g_c^{ani} are predicted for each mode through a quantitative comparison of the Cauchy stress versus the amount of shear curves of the simulation results with those of the corresponding experiments. The elastic and the crack-field parameters for simple shear are summarized in Table 3. Here the mechanical response of the tissue is also assumed to be elastic up to the ultimate stress yielding the aforestated elastic material parameters.

Fig. 11 shows the finite element results in terms of the Cauchy stress ($\sigma_{z\theta}$ and $\sigma_{\theta z}$) versus the amount of shear (γ) and they agree well with the anisotropic experimental response. It needs to be underlined that the numerical results provided in Fig. 11 are obtained by considering the average of all nodal stresses at the edge $z = \theta = 3$ mm for the $z\theta$ mode, and at the edge $\theta = 3$, $z = 5$ mm for the θz mode. The onset of the cracks is observed at the two tips of
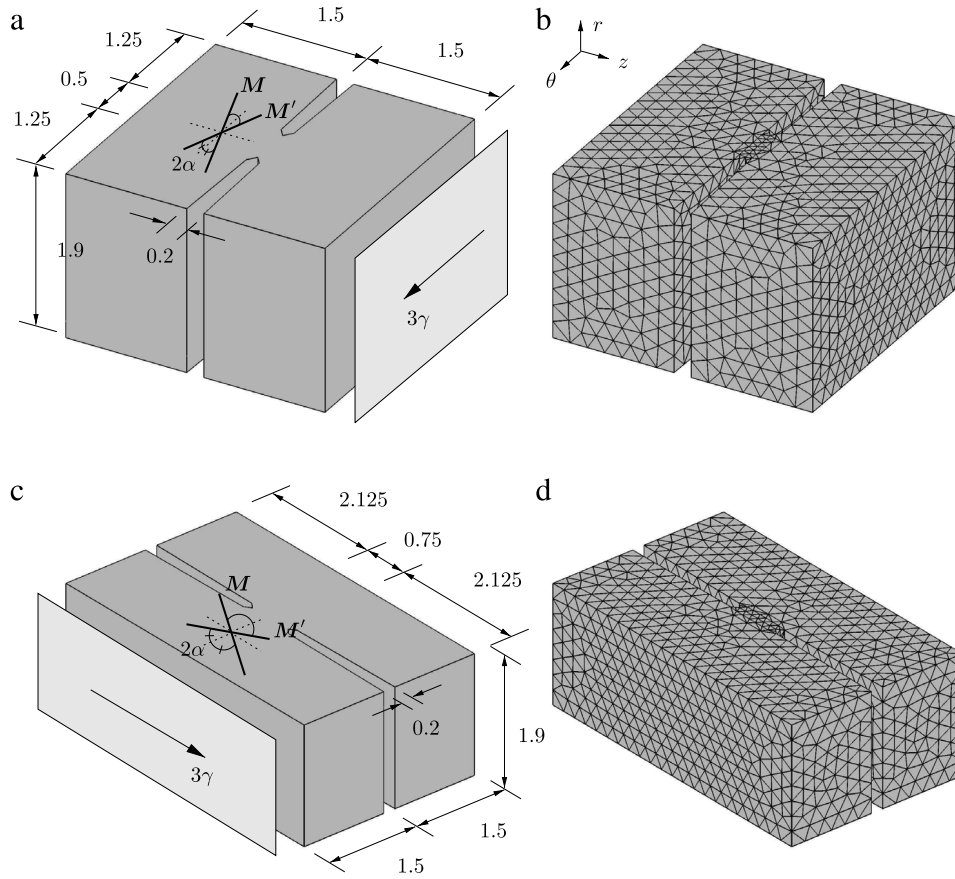
Fig. 10. (a), (c) Geometries of the specimens sheared in the circumferential θ-direction ($z\theta$ mode) and in the longitudinal z-direction (θz mode) by the displacement 3γ (thickness times amount of shear). The structure of the media is characterized by two families of fibers, oriented in the directions M and M' in the reference configuration, corresponding to the collagenous component of the material, and they are symmetrically arranged with respect to the cylinder axis — α is the angle between the fibers and the circumferential direction; (b), (d) related finite element meshes of the corresponding geometries with refinements around the incisions. Dimensions are provided in millimeters.
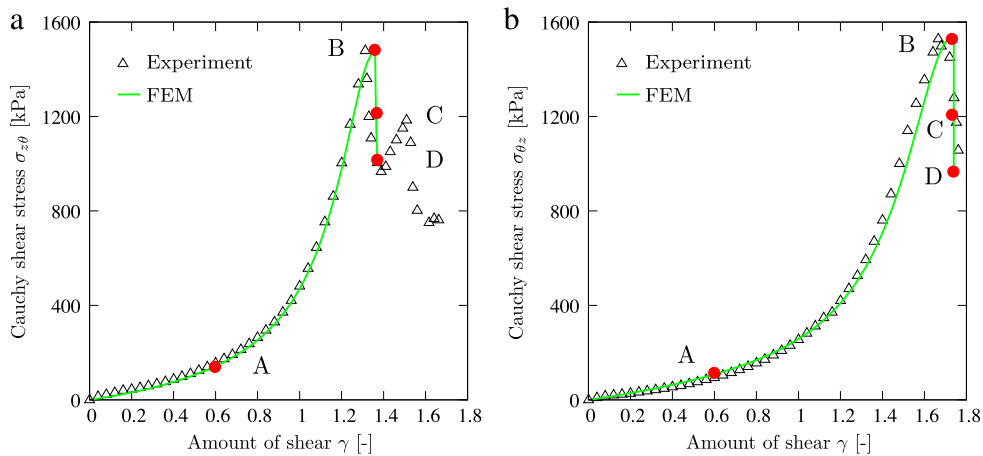

Fig. 11. Simple shear test data (triangles) and corresponding finite element results (solid curves): (a) Cauchy shear stress $\sigma_{z\theta}$ versus amount of shear γ for the $z\theta$ mode; (b) Cauchy shear stress $\sigma_{\theta z}$ versus γ for the θz mode.
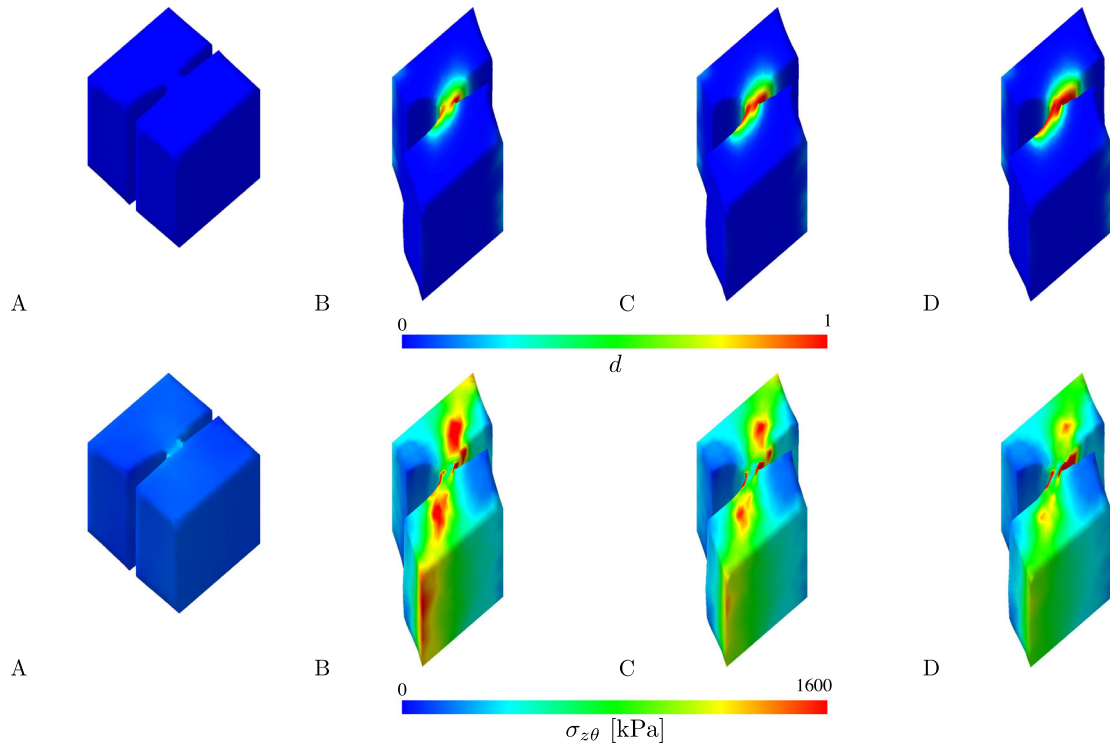
Fig. 12. Distributions of the finite element results of simple shear in the circumferential θ-direction ($z\theta$ mode) with anisotropic failure at the locations A–D according to Fig. 11(a): (above) distribution of crack phase-field d; (below) corresponding Cauchy shear stress $\sigma_{z\theta}$.

the symmetrically incised region where the stress concentration, and therefore, the energy of the intact tissue satisfies the failure condition. The two distinct crack patterns meet in the middle of the refined region at which the complete failure phenomenon manifests itself. This is accompanied by the sudden loss of the load-bearing capacity as depicted in the corresponding curves of the Cauchy shear stress versus the amount of shear, see Fig. 11. Fig. 12 illustrates the distributions of the crack phase-field d and the Cauchy shear stress $\sigma_{z\theta}$ at the locations A–D (indicated in Fig. 11(a)), while the crack phase-field d and the shear stress $\sigma_{\theta z}$ at the four states (according to Fig. 11(b)) are displayed in Fig. 13.

7. Discussion

In this study we have proposed a new anisotropic crack phase-field approach to model failure of aortic tissues undergoing finite deformation. An anisotropic invariant-based hyperelastic model along with the phase-field model of fracture describe the elastic mechanical behavior of the tissue and the associated crack growth, respectively. The evolution of the crack phase-field was constructed on the basis of two critical fracture energies, one for the ground matrix and the other one for the collagen fibers. On the theoretical side, the multi-field problem was established on a rate-type variational principle, while on the numerical side the time-discrete incremental counterpart of the rate-type variational principle was replaced by a Galerkin-type weak formulation where the staggered finite element formulation was employed for a quasi-static process.

On the constitutive part, the aortic tissue (in this study it is the media) is treated as a fiber-reinforced material with the fibers corresponding to the collagenous component of the material and symmetrically disposed with respect to the cylinder axis; the used constitutive law is nonlinear and anisotropic. The evolution of the crack phase-field is dictated by an energy-based anisotropic failure criterion using critical fracture energies which relate to the ground matrix and the collagen fibers, as emphasized in Section 4.2. In addition, we also focused on the numerical implementation of the model and, finally, present quantitative comparisons of simulation results with experimental data that substantiate our modeling endeavors.
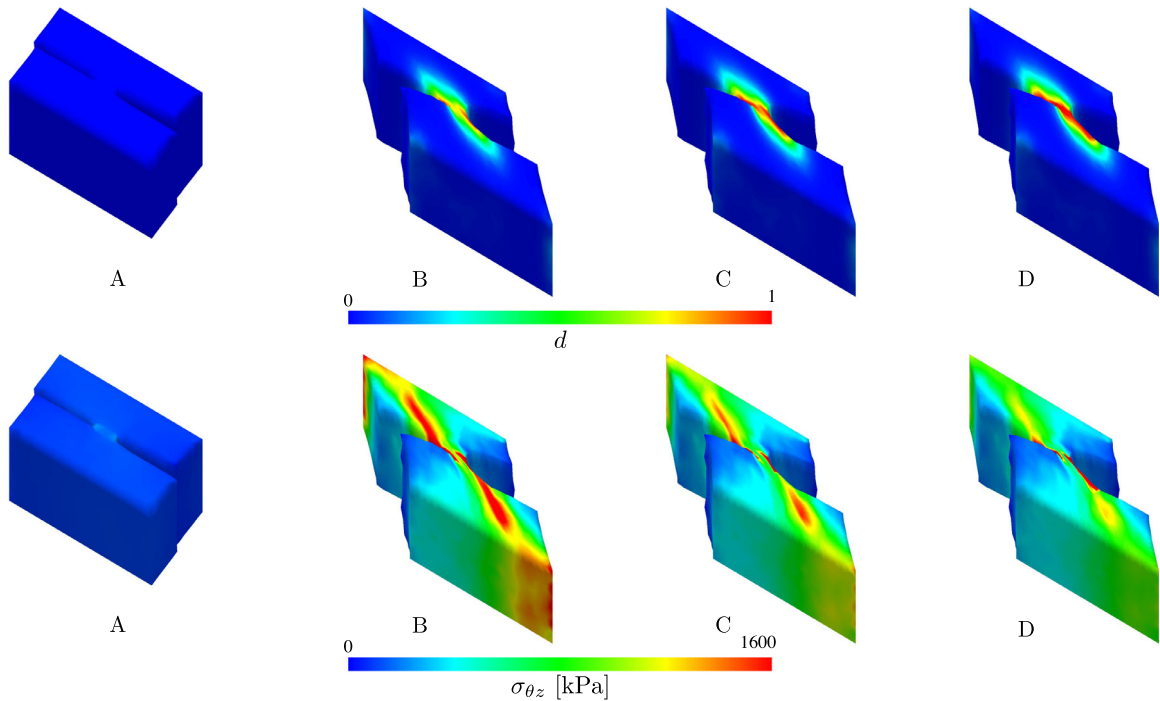
Fig. 13. Distributions of the numerical results of simple shear in the longitudinal z-direction (θz mode) with anisotropic failure at the locations A–D according to Fig. 11(b): (above) distribution of crack phase-field d; (below) corresponding Cauchy shear stress $\sigma_{\theta z}$.

Aortic tissues are structurally comparable to fiber-reinforced composites. The mechanical behavior of the tissue before and after the onset of a crack is strongly dependent on the heterogeneities of the material, i.e. regional variations of tissue components such as collagen and elastin, existence of micro-defects, micro-calcification, etc. [28,60,61]. Accordingly, the hyperelastic constitutive model and the failure criterion presented here can be modified in order to consider the tissue micro-structure,e.g., histologically related parameters such as the density and dispersion of collagen fibers. In particular, the dispersion of collagen fibers both in-plane and out-of-plane, see [10] for more details, may considerably affect the failure mechanism. In addition, in order to shape the overall mechanical response of the tissue the role of collagen cross-links and proteoglycans should not be overlooked.

Tissue failure often occurs within different loading steps, i.e. in a typical stress–stretch curve two, sometimes more peaks can be observed until complete rupture. Thereby, the rupture of one fiber bundle is followed by the other; see, e.g., the experimental shear data ($z\theta$ mode) illustrated in Fig. 11(a). In a sense, this evokes a distinct evolution of the crack phase-field in regard to each fiber family, as suggested in [45]. The experimental tissue data of the post-cracking behavior, i.e. the mechanical response of the tissue beyond reaching the ultimate stress until complete rupture, show also a considerable variability, see, e.g., Fig. 11. An alternative modeling approach which may increase the numerical accuracy is the use of a higher-order phase-field model, see, e.g., [46]. That allows to capture the fracture of highly anisotropic solids at finite strains. One of the criticisms of the presented model may be the choice of the elastic material parameters that render two different parameter sets, compare with Tables 2 and 3. We hereby point out that the fusion of the uniaxial extension and shear test data, at least for the experimental data set we use, was not satisfactory, albeit we tried to minimize one objective function involving the sum of squares of both uniaxial and shear responses. In other words we were not able to find one set of elastic parameters which was able to mimic both tests. The same unsatisfactory results were observed by trying to use one set of $g_{\mathrm{c}}^{\mathrm{iso}}$ and $g_{\mathrm{c}}^{\mathrm{ani}}$ throughout the finite element simulations.

We note that in the presented study we focused on the mechanical response of the medial tissue, treated as a solid, and we entirely neglect the intricate feed-back mechanism between the mechanical and the biochemical environment of the tissue known as *mechanotrandsduction*. Nevertheless, the presented approach with the aforementioned phenomenological and structurally motivated enhancements provides the basis to model fracture of soft biological

tissues, in particular of aortic tissues, which may occur in pathologies such as aneurysms and atherosclerotic plaques but also in healthy tissues due to impact loads that may occur during an accident.

Acknowledgments

Appendix

A.1. Derivation of the Euler–Lagrange equations (25)

The minimization principle (23) can be interpreted as the first variation of the regularized crack surface $\delta \Gamma_l(d)$ to be equal to zero. With the use of (21) and (22) we obtain

$$\delta \Gamma_l(d) = \partial_d \, \Gamma_l(d) \, \delta d + \partial_{\nabla d} \Gamma_l(d) \nabla \delta d$$
$$= \frac{1}{l} \int_{\mathcal{B}} (d \, \delta d + l^2 \nabla d \cdot \nabla \delta d) \mathrm{d}V = 0. \tag{73}$$

Let us now focus on the second term in $(73)_2$. The exploitation of the product rule gives

$$\int_{\mathcal{B}} l^2 \nabla d \cdot \nabla \delta d \mathrm{d}V = l^2 \int_{\mathcal{B}} Div(\nabla d \, \delta d) \mathrm{d}V - l^2 \int_{\mathcal{B}} \Delta d \, \delta d \mathrm{d}V, \tag{74}$$

and the Gaussian integral theorem provides

$$\int_{\mathcal{B}} l^2 \nabla d \cdot \nabla \delta d \, \mathrm{d}V = l^2 \int_{\partial \mathcal{B}} \nabla d \cdot N \delta d \mathrm{d}A - l^2 \int_{\mathcal{B}} \Delta d \, \delta d \, \mathrm{d}V \tag{75}$$

so that from $(73)_2$ we obtain

$$\delta \Gamma_l(d) = \frac{1}{l} \int_{\mathcal{B}} (d - l^2 \Delta d) \delta d \mathrm{d}V + l \int_{\partial \mathcal{B}} \nabla d \cdot N \delta d \, \mathrm{d}A = 0. \tag{76}$$

For any δd this relation is zero when $d - l^2 \Delta d = 0$ in $\mathcal{B}$ and $\nabla d \cdot N = 0$ on $\partial \mathcal{B}$, which is the requested result (25).

References

[1] G.A. Holzapfel, T.C. Gasser, R.W. Ogden, A new constitutive framework for arterial wall mechanics and a comparative study of material models, J. Elasticity 61 (2000) 1–48.
[2] B. Alberts, A. Johnson, J. Lewis, M. Raff, K. Roberts, P. Walter, Molecular Biology of the Cell, fifth ed., Garland Science, New York, 2008.
[3] J.D. Humphrey, Cardiovascular Solid Mechanics. Cells, Tissues, and Organs, Springer-Verlag, New York, 2002.
[4] F. Schmid, G. Sommer, M. Rappolt, C.A.J. Schulze-Bauer, P. Regitnig, G.A. Holzapfel, P. Laggner, H. Amenitsch, In situ tensile testing of human aortas by time-resolved small angle X-ray scattering, Synchro. Rad. 12 (2005) 727–733.
[5] T.C. Gasser, R.W. Ogden, G.A. Holzapfel, Hyperelastic modelling of arterial layers with distributed collagen fibre orientations, J. R. Soc. Interface 3 (2006) 15–35.
[6] L. Yang, K.O. van der Werf, P.J. Dijkstra, J. Feijen, M.L. Bennink, Micromechanical analysis of native and cross-linked collagen type I fibrils supports the existence of microfibrils, J. Mech. Behav. Biomed. Mater. 6 (2012) 148–158.
[7] A. Delfino, N. Stergiopulos, J.E. Moore Jr., J.-J. Meister, Residual strain effects on the stress field in a thick wall finite element model of the human carotid bifurcation, J. Biomech. 30 (1997) 777–786.
[8] H. Demiray, R.P. Vito, A layered cylindrical shell model for an aorta, Internat. J. Engrg. Sci. 29 (1991) 47–54.
[9] Y.C. Fung, K. Fronek, P. Patitucci, Pseudoelasticity of arteries and the choice of its mathematical expression, Am. J. Physiol. 237 (1979) H620–H631.
[10] G.A. Holzapfel, J.A. Niestrawska, R.W. Ogden, A.J. Reinisch, A.J. Schriefl, Modelling non-symmetric collagen fibre dispersion in arterial walls, J. R. Soc. Interface 12 (2015) 20150188.
[11] V. Alastrué, M.A. Martinez, M. Doblaré, A. Menzel, Anisotropic micro–sphere–based finite elasticity applied to blood vessel modelling, J. Mech. Phys. Solids 57 (2009) 178–203.
[12] J.E. Bischoff, E.M. Arruda, K. Grosh, A microstructurally based orthotropic hyperelastic constitutive law, J. Appl. Mech. 69 (2002) 570–579.

[13] G.A. Holzapfel, R.W. Ogden, Constitutive modelling of arteries, Proc. R. Soc. Lond. Ser. A Math. Phys. Eng. Sci. 466 (2010) 1551–1597.
[14] J.D. Humphrey, G.A. Holzapfel, Mechanics, mechanobiology, and modeling of human abdominal aorta and aneurysms, J. Biomech. 45 (2012) 805–814.
[15] J.H. Kim, S. Avril, A. Duprey, J.P. Favre, Experimental characterization of rupture in human aortic aneurysms using a full-field measurement technique, Biomech. Model. Mechanobiol. 11 (2012) 841–853.
[16] Y.S. Chatzizisis, A.Ü Coşkun, M. Jonas, E.R. Edelman, C.L. Feldman, P.H. Stone, Role of endothelial shear stress in the natural history of coronary atherosclerosis and vascular remodeling: molecular, cellular, and vascular behavior, J. Am. Coll. Cardiol. 49 (2007) 2379–2393.
[17] K.S. Cunningham, A.I. Gotlieb, The role of shear stress in the pathogenesis of atherosclerosis, Lab. Invest. 85 (2005) 9–23.
[18] G.A. Holzapfel, G. Sommer, P. Regitnig, Anisotropic mechanical properties of tissue components in human atherosclerotic plaques, J. Biomech. Eng. 126 (2004) 657–665.
[19] F.J. Criado, Aortic dissection: a 250-year perspective, Tex. Heart Inst. J. 38 (2011) 694–700.
[20] T.C. Gasser, G.A. Holzapfel, Modeling the propagation of arterial dissection, Eur. J. Mech. A Solids 25 (2006) 617–633.
[21] T. Belytschko, T. Black, Elastic crack growth in finite elements with minimal remeshing, Interat. J. Numer. Methods Engrg 45 (1999) 601–620.
[22] N. Moës, T. Belytschko, Extended finite element method for cohesive crack growth, Eng. Fract. Mech. 69 (2002) 813–833.
[23] N. Moës, J. Dolbow, T. Belytschko, A finite element method for crack growth without remeshing, Int. J. Numer. Meth. Engng 46 (1999) 131–150.
[24] A. Ferrara, A. Pandolfi, Numerical modeling of fracture in human arteries, Comput. Methods Biomech. Biomed. Eng. 11 (2008) 553–567.
[25] M. Ortiz, A. Pandolfi, Finite-deformation irreversible cohesive elements for three-dimensional crack-propagation analysis, Int. J. Numer. Meth. Engng 44 (1999) 1267–1282.
[26] A. Ferrara, A. Pandolfi, A numerical study of arterial media dissection processes, Int. J. Fract. 166 (2010) 21–33.
[27] A. Raina, C. Miehe, A phase-field model for fracture in biological tissues, Biomech. Model. Mechanobiol. (2016) in press.
[28] M.F. Hadi, E.A. Sander, V.H. Barocas, Multiscale model predicts tissue-level failure from collagen fiber-level damage, J. Biomech. Eng. 134 (2012) 1–10.
[29] T.I. Zohdi, A computational framework for network modeling of fibrous biological tissue deformation and rupture, Comput. Methods Appl. Mech. Engrg. 196 (2007) 2972–2980.
[30] D. Balzani, S. Brinkhues, G.A. Holzapfel, Constitutive framework for the modeling of damage in collagenous soft tissues with application to arterial walls, Comput. Methods Appl. Mech. Engrg. 213–216 (2012) 139–151.
[31] L.M. Kachanov, Introduction to Continuum Damage Mechanics, Martinus Nijhoff Publishers, Dordrecht, The Netherlands, 1986.
[32] T. Schmidt, D. Balzani, G.A. Holzapfel, Statistical approach for a continuum description of damage evolution in soft collagenous tissues, Comput. Methods Appl. Mech. Engrg. 278 (2014) 41–61.
[33] T. Schmidt, D. Balzani, Relaxed incremental variational approach for the modeling of damage-induced stress hysteresis in arterial walls, J. Mech. Behav. Biomed. Mater. 58 (2016) 149–162.
[34] D. Balzani, M. Ortiz, Relaxed incremental variational formulation for damage at large strains with application to fiber-reinforced materials and materials with truss-like microstructures, Int. J. Numer. Meth. Engng 92 (2012) 551–570.
[35] J. Skrzypek, A. Ganczarski, Modeling of Material Damage and Failure of Structures, Springer Verlag, Berlin, 1999.
[36] A.A. Griffith, The phenomena of rupture and flow in solids, Phil. Trans. R. Soc. A 221 (1921) 163–197.
[37] G.R. Irwin, Fracture mechanics, in: J.N. Goodier, N.J. Hoff (Eds.), Structural Mechanics, Pergamon Press, New York, 1960, pp. 557–594.
[38] G.A. Francfort, J.-J. Marigo, Revisiting brittle fracture as an energy minimization problem, J. Mech. Phys. Solids 46 (1998) 1319–1342.
[39] B. Bourdin, G.A. Francfort, J.-J. Marigo, Numerical experiments in revisited brittle fracture, J. Mech. Phys. Solids 48 (2000) 797–826.
[40] D. Mumford, J. Shah, Optimal approximations by piecewise smooth functions and associated variational problems, Comm. Pure Appl. Math. 42 (1989) 577–685.
[41] A. Braides, Gamma-Convergence for Beginners, Oxford University Press, New York, 2002.
[42] B. Bourdin, G.A. Francfort, J.-J. Marigo, The Variational Approach to Fracture, Springer-Verlag, Berlin, 2008.
[43] V. Hakim, A. Karma, Laws of crack motion and phase-field models of fracture, J. Mech. Phys. Solids 57 (2009) 342–368.
[44] C. Miehe, F. Welschinger, M. Hofacker, Thermodynamically consistent phase-field models of fracture: variational principles and multi-field fe implementations, Int. J. Numer. Meth. Engng 83 (2010) 1273–1311.
[45] O. Gültekin, A phase field approach to the fracture of anisotropic medium (Master's thesis), University of Stuttgart, Institute of Applied Mechanics (CE), Pfaffenwaldring 7, Stuttgart, 2014.
[46] B. Li, C. Peco, D. Millán, I. Arias, M. Arroyo, Phase-field modeling and simulation of fracture in brittle materials with strongly anisotropic surface energy, Int. J. Numer. Meth. Engng 102 (2015) 711–727.
[47] C. Miehe, M. Hofacker, F. Welschinger, A phase field model for rate-independent crack propagation: robust algorithmic implementation based on operator splits, Comput. Methods Appl. Mech. Engrg. 199 (2010) 2765–2778.
[48] G. Sommer, S. Sherifova, P.J. Oberwalder, O.E. Dapunt, P.A. Ursomanno, A. DeAnda, B.E. Griffith, G.A. Holzapfel, Mechanical strength of aneurysmatic and dissected human thoracic aortas at different shear loading modes, J. Biomech. (2016) in press.
[49] J.E. Marsden, T.J.R. Hughes, Mathematical Foundations of Elasticity, Dover, New York, 1994.
[50] A.N. Annaidh, M. Destrade, M.D. Gilchrist, J.G. Murphy, Deficiencies in numerical models of anisotropic nonlinearly elastic materials, Biomech. Model. Mechanobiol. 12 (2013) 781–791.
[51] D.R. Nolan, A.L. Gower, M. Destrade, R.W. Ogden, J.P. McGarry, A robust anisotropic hyperelastic formulation for the modelling of soft tissue, J. Mech. Behav. Biomed. Mater. 39 (2014) 48–60.
[52] J. Helfenstein, M. Jabareen, E. Mazza, S. Govindjee, On non-pyhsical response in models for fiber-reinforced hyperelastic materials, Int. J. Solids Struct. 47 (2010) 2056–2061.
[53] G.A. Holzapfel, Nonlinear Solid Mechanics. A Continuum Approach for Engineering, John Wiley & Sons, Chichester, 2000.

[54] C. Miehe, Aspects of the formulation and finite element implementation of large strain isotropic elasticity, Int. J. Numer. Meth. Engng 37 (1994) 1981–2004.

[55] J.C. Simo, R.L. Taylor, Quasi-incompressible finite elasticity in principal stretches. Continuum basis and numerical algorithms, Comput. Methods Appl. Mech. Engrg. 85 (1991) 273–310.

[56] U. Heisserer, S. Hartmann, A. Düster, Z. Yosibash, On volumetric locking-free behaviour of p-version finite elements under finite deformations, Commun. Numer. Methods. Eng. 24 (2008) 1019–1032.

[57] G. Sommer, T.C. Gasser, P. Regitnig, M. Auer, G.A. Holzapfel, Dissection properties of the human aortic media: an experimental study, J. Biomech. Eng. 130 (2008) 021007–1–12.

[58] T.J.R. Hughes, The Finite Element Method: Linear Static and Dynamic Finite Element Analysis, Dover, New York, 2000.

[59] P. Wriggers, Nonlinear Finite Element Methods, Springer-Verlag, Berlin, Heidelberg, 2008.

[60] J.W. Hutchinson, Z. Suo, Mixed mode cracking in layered materials, Adv. Appl. Math. 29 (1991) 63–191.

[61] J.D. Hutcheson, C. Goettsch, S. Bertazzo, N. Maldonado, J.L. Ruiz, W. Goh, K. Yabusaki, T. Faits, C. Bouten, G. Franck, T. Quillard, P. Libby, M. Aikawa, S. Weinbaum, E. Aikawa, Genesis and growth of extracellular-vesicle-derived microcalcification in atherosclerotic plaques, Nature Mater. 15 (2016) 335–343.